International Journal of Pharmaceutics 573 (2020) 118802

Contents lists available at ScienceDirect

International Journal of Pharmaceutics

journal homepage: www.elsevier.com/locate/ijpharm

Engineered extracellular vesicles with synthetic lipids *via* membrane fusion to establish efficient gene delivery

Yong-Yu Jhan, Daniel Prasca-Chamorro, Guillermo Palou Zuniga, David Mitchell Moore, Shreedevi Arun Kumar, Akhilesh K. Gaharwar, Corey J. Bishop*

Department of Biomedical Engineering, Texas A&M University, Texas, USA

ARTICLE INFO

Keywords:
RNAi therapeutics
Membrane fusion
Exosomes
Hybridized extracellular vesicles
Extracellular vesicle mimetic
Anti-cancer
Gene delivery

ABSTRACT

The low yield of extracellular vesicle (EV) secretion is a major obstacle for mass production and limits their potential for clinical applications as a drug delivery platform. Here, we mass produced engineered extracellular vesicles (eEVs) by fusing the surface composition of EVs with lipid-based materials via a membrane extrusion technique. A library of lipids (DOTAP, POPC, DPPC and POPG) was fused with EVs to form a hybrid-lipid membrane structure. Uniform lamellar vesicles with a controlled size around 100 nm were obtained in this study. Particle number characterization revealed this extrusion method allowed a 6- to 43-fold increase in numbers of vesicles post- isolation. Further, exogenous siRNA was successfully loaded into engineered vesicles with ~ 15% – 20% encapsulation efficiency using electroporation technique. These engineered extracellular vesicles sustained a 14-fold higher cellular uptake to lung cancer cells (A549) and achieved an effective gene silencing effect comparable to commercial Lipofectamine RNAiMax. Our results demonstrate the surface composition and functionality of EVs can be tuned by extrusion with lipids and suggest the engineered vesicles can be a potential substitute as gene delivery carriers while being able to be mass produced to a greater degree with retained targeting capabilities of EVs.

1. Introduction

The delivery of RNA molecules (*i.e.* short interfering RNA (siRNA), microRNA (miRNA), short hairpin RNA (shRNA)) to silence aberrant expression of genes in a cell is a potentially powerful therapeutic strategy for a variety of diseases and cancer in recent decades. Inducing RNA interference (RNAi) (Ruigrok et al., 2016) by the delivery of exogenous small RNA molecules as a therapeutic holds great promise for anti-cancer applications (Charoenphol et al., 2018), as the RNAi process can inactivate specific oncogenes or inhibit cell migration or cell growth (Lee et al., 2016). Despite the great therapeutic opportunities of siRNA, due to the inherent characteristics of siRNA, effective delivery of siRNA into target cells is the key challenge remaining to be resolved by the RNAi scientific community. Owing to the molecular weight (~13–14 kDa) and highly negatively-charged phosphate backbone of siRNA, naked siRNA cannot efficiently traverse the cell membrane (Kim et al., 2015). In addition, siRNA is vulnerable to enzymatic degradation by prevalent RNases within the *ex vivo* and *in vivo* environment. Although chemical modifications help RNA stability, superior small RNA molecule delivery carriers must be engineered.

Extracellular vesicles (EVs), such as exosomes and microvesicles, have been acknowledged for their potential use as a therapeutic for the past 17 years (Gilligan and Dwyer, 2017; Harding et al., 2013; Jiang (2017b)). EVs are naturally secreted by most cell types. Typically, exosomes, which is a sub-population of EVs, are in the range of 30 – 150 nm in diameter (Andaloussi et al., 2013b; Srivastava et al., 2016). These vesicles have been uncovered to function as intercellular communicators that shuttle a variety of cargo, particularly miRNAs, to local cells or distant tissues (Maas et al., 2017). They are able to direct their cargo to specific recipient cells, which holds great promise for exploiting EVs as targeting, drug and gene delivery vehicles. Since EVs are phospholipid structures and exhibit surface marker/protein ligands on their membranes, they can potentially overcome biological barriers and reduce off-target effects within the body (Andaloussi et al., 2013a; Maheshwari et al., 2017). Increasingly more studies have indicated EVs present fewer safety issues compared to cell therapy strategies or other conventional drug delivery systems (Jiang and Gao (2017a)). Furthermore, EVs' functionality can be tailored by manipulating their cell sources, or endogenous tailoring through genetic or metabolic engineering, or by exogenous tailoring methods involving packing

* Corresponding author at: Department of Biomedical Engineering, Texas A&M University, Texas 77840, USA.
E-mail address: coreyjbishop@tamu.edu (C.J. Bishop).

https://doi.org/10.1016/j.ijpharm.2019.118802
Received 16 July 2019; Received in revised form 11 October 2019; Accepted 13 October 2019
Available online 09 November 2019
0378-5173/

payloads post-isolation of the vesicles (Armstrong et al., 2017; Luan et al., 2017). These versatile capabilities of EVs lend credence to their potential as cell-free, active targeting vehicles for a variety of RNA therapeutics.

Excitingly, Alnylam recently received the first U.S. FDA approval for a sugar (GalNAc)-based RNAi formulation, which opens the door for 510(k) clearances. However, despite intense EV studies within a wide range of RNAi therapeutic applications (Ohno et al., 2016; Vader et al., 2016), most of the EV-related clinical trials have begun in the last 5 years, thus most clinical trials are in phase I/II (Conlan et al., 2017). One of the major hurdles is the lack of cost-effective methods to obtain sufficient quantities of EVs with consistent biochemical characteristics for clinical application (Armstrong and Stevens, 2018; Fuhrmann et al., 2018). There is difficulty in scaling up EVs from a manufacturing standpoint; the yields for EV isolation and purification from *in vitro* cell culture are extremely low and often impractical. Moreover, the abilities to develop a stable, effective, and more scalable extracellular vesicle-based formulation which can be loaded with exogenous cargo remains elusive. A potential solution to help clinically translate siRNA delivery therapeutics could be integrating synthetic/exogenous lipids into already-isolated EVs to help control the physicochemical properties and the mass production. However, by doing so, the EVs' targeting functionality may decrease as the density of the endogenous protein decreases. We hope to balance these two trade-offs, while ensuring both are sufficient for a given application. In this study, we report an engineering approach to mass produce lipid-doped extracellular vesicles post-EV isolation by generating synthetic lipid-hybridized EVs. The physicochemical properties and functionalities of our hybridized EVs have been thoroughly characterized and are described herein.

2. Material and methods

2.1. Materials

Please refer to the *Supporting Information* for material details.

2.2. Methods

2.2.1. Extracellular vesicle induction and isolation

3 T3 and A549 cells were grown with complete media until ~ 100% confluent. The media was removed from the culturing flasks and the flasks were washed with phosphate-buffered saline (PBS) twice to remove any remaining media. After which, the cells were continued to be cultured in FBS-depleted media for 48 hr to promote the secretion of EVs. The conditioned media was collected and the EVs were isolated by serial centrifugation at 4 °C (Greening et al., 2015; Szatanek et al., 2015), using a TX150 rotor and ST8 centrifuge. The media was centrifuged at 300 g for 10 min., 2,000 g for 20 min., and 10,000 g for 30 min. The first, second, and last centrifugations were to remove intact cells, dead cells, and cell debris, respectively. Note that the pellet was discarded after each centrifugation. The supernatant media was then transferred to ultracentrifuge tubes and centrifuged at 125,000 g (Beckman Coulter centrifuge with TLA-55 rotor) for 70 min at 4 °C. The pellet was resuspended in PBS, then filtered using a low protein binding polyvinylidene fluoride (PVDF) 0.22 μm filter. The isolated EVs were stored at a concentration of 10^{10} particles/ml at −20 °C. To remove unwanted non-vesicular particles, OptiPrep™ density gradient solutions (Sigma, #D1556) were used to separate particles by their density (exosome: 1.1–1.19 g/ml) according to literature (Greening et al., 2015). In our small-scale preparation, no significant difference of protein: lipid ratios between the samples using ultracentrifugation and OptiPrep™ density gradient centrifugation were observed, however.

2.2.2. Engineered extracellular vesicles via extrusion

The eEVs were fused using a serial extrusion technique (Scheme 1). The lipid solutions were dissolved in chloroform (10 mM) according to literature (Sato et al., 2016). The organic solvent was evaporated in a vacuum chamber to yield a thin lipid film on the bottom of a glass vial. The lipid film was then hydrated by adding a PBS buffer. Prior to membrane extrusion, the lipid solutions were heated at a temperature above their phase transition temperature and vortexed until they were visually homogeneous. The phase transition temperature of each individual lipid is shown in **Fig. S1**. The extracellular vesicles were subsequently warmed to 37 °C. The lipid: EV solutions were mixed at varying volumetric ratios (9:1, 4:1, 1:1); the lipid solution was at a concentration of 5 mM and the EV concentration was 1.5×10^{10} particles/ml (or 50 μg/ml of protein according to a Micro BCA assay. The mixtures were vortexed and sonicated for 2 min using a 120 Watt, 20 kHz sonicator (Fisher Scientific FB120) at 20% max amplitude to fully solvate the solution. Subsequently, the mixtures were serially extruded through pore sizes of 400 nm, 200 nm, and then 100 nm. For each extrusion procedure, the mixtures were push forward and backward manually more than 25 times according to the manufacturer's instruction (T&T Scientific) (Scheme 1).

2.2.3. Physicochemical quantification of EVs from cells and eEVs

2.2.3.1. Membrane protein quantification assay. The total quantity of protein within EVs was quantified via a Micro BCA Protein Assay Kit, according to the manufacturer's instructions. Briefly, a set of protein standards were prepared within the linear working range of 2–40 μg/ml. EV samples with different concentration were mixed with working solution in a 96 well microplate and incubated at 37 °C for 2 hr. Absorbance in each well was measured using a plate reader (Cytation 5, BioTek Instruments, Inc.) at 562 nm.

2.2.3.2. Flow cytometry – Characterization of EV surface marker and purity. EVs obtained after differential centrifugation and filtration were then analyzed by flow cytometry for the presence of exosome marker CD63 (Löf et al., 2016; Properzi et al., 2013). Initially, EVs were diluted to the concentration of 5000 ng of affiliated protein or a total 10^{10} particles in 50 μl of PBS solution. The solutions were subsequently mixed with 0.125 μg (1.25 μl) of anti-CD63-eFluor 660 antibodies to a final volume of 100 μl of PBS with 0.2% bovine serum albumin (BSA) blocking solution. The mixture was incubated at room temperature for 30 min. in the dark before conducting flow cytometry analysis. Flow cytometry was accomplished using a BD Accuri™ C6 Cytometer at a flow rate of 11 μl/min. Auto-fluorescence was quantified using the samples in the absence of the anti-CD63-conjugated eFluor 660 antibody. POPC, which has no CD63 surface marker expression, was used to identify the background fluorescence *via* flow cytometry for gating purposes. To characterize the percentage of CD63 expressing vesicles or the percentage of EVs within our solution, the percentage of eFluor 660 fluorescence was quantified using the FL4-H channel.

2.2.3.3. Nanoparticle tracking analysis – size, concentration and production yield. The size and concentration of exosomes were characterized by nanoparticle tracking analysis (NTA) (Malvern NanoSight LM10, Amesbury, United Kingdom). An appropriate working concentration in the measurable range of 10^8 particles/ml was used to determine the original concentration of EVs. The EV samples with serial diluted concentrations (in PBS) were injected in the NTA sample chamber using sterile syringes. Data for each sample were collected for 60 s at room temperature and analyzed using NanoSight NTA 3.2 software. Three individual measurements of each condition were performed immediately after the sample was injected into the chamber. The error bars shown are standard deviations of the mean size and the original concentration was calculated using a dilution factor. A dilution factor was necessary to be within the measurable concentration range for NTA (10^{7-9} particles/ml). The production yield of EVs was further normalized to the cell number per flask (or dish) at ~ 100% confluency, counted by hemocytometer. Likewisely, an appropriate working concentration of eEVs in the NTA measurable range of 10^8

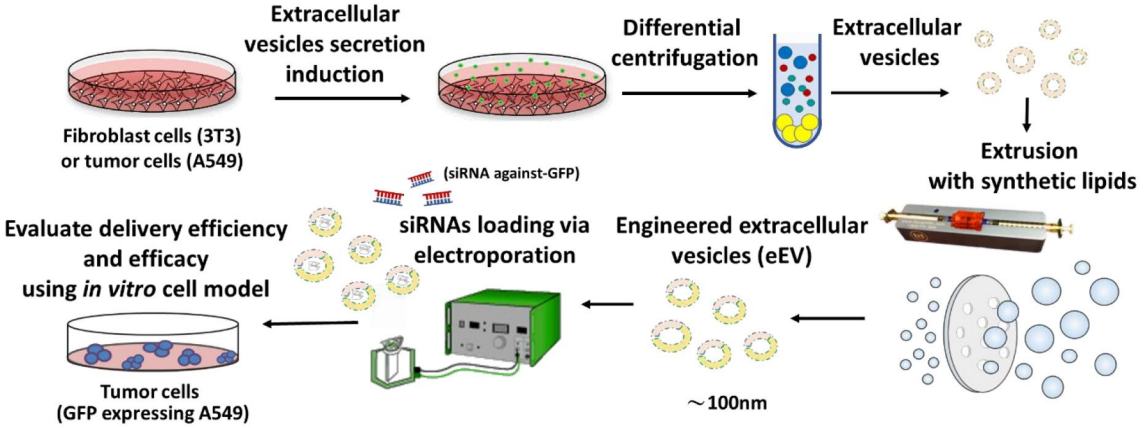

Scheme 1. Schematic illustration of the procedure for the generation of engineered lipid/extracellular vesicles (EVs).

particles/ml was prepared to determine the size and concentration of eEVs. The concentration of eEVs were normalized to the concentration of native EVs to quantify the production yield, in terms of the fold increase of eEVs.

2.2.3.4. Transmission electron microscopy – morphology. A pellet of EVs or eEVs (~10^8 particles) was resuspended in 50 µl of PBS and stained on Formvar/carbon-coated copper grid for microscopy imaging purposes following the protocol in previous literature (Théry et al., 2006). Details of the steps for sample staining are depicted in *Supporting Information*. A drop of 5 – 10 µl of EV suspension was put on clean Parafilm. The sample grids were then allowed to vacuum dry overnight and observed *via* TEM (JEOL 1200EX) under 100 kV of energy and 100,000x to 150,000x magnification.

2.2.3.5. Zeta potential measurements. To obtain information about the stability of the vesicles in terms of particle aggregation and flocculation, the zeta potentials of the vesicles were evaluated measured in PBS and water. The zeta potential of vesicles was measured using a Zetasizer (NanoZS) from Malvern Instruments with a detection angle of 173° and laser wavelength of 633 nm (cuvette: ZEN0040). 10 µg/ml (affiliated protein concentration) of EV and 10^9–10^{10} particles/ml of eEVs were used for the measurements.

2.2.4. Quantifying native EV fraction within eEVs for validating membrane incorporation

2.2.4.1. Membrane composition quantification assay. To validate the membrane incorporation of lipids to extracellular vesicles, we conducted membrane composition analysis to quantitatively evaluate the efficiency of membrane fusion. Osteikoetxea, X., *et al.* demonstrated that the protein to lipid ratios characteristic could be a consistent parameter to characterize extracellular vesicles populations (Osteikoetxea et al., 2015). Therefore, we quantify the EV fraction within eEVs by quantifying the protein (which is EV-derived) and the lipid content (which is both EV- and synthetic lipid-derived) within. The protein quantification method (Micro BCA) was described previously in "*Membrane protein quantification assay*". A sulfo-phospho-vanillin (SPV) assay was used following previous protocol (Osteikoetxea et al., 2015). Details of the steps for lipid quantification are depicted in *Supporting Information*. Total protein to total lipid ratios were further calculated to determine the fusion efficiency of exosomal membrane. To confirm the lipid molecules presenting in the samples did not interfere with the total protein determination in terms of causing false-positive protein results, we tested the pure lipid solution for their assay interference with the protein determination, followed by quantification of the total protein to lipid ratios for pure lipid solution.

2.2.4.2. Flow cytometry-based eEV/EV ratio quantification assay. To quantify the native EV portion within the eEVs, anti-CD63 conjugated eFluor 660 antibody was used as a labeling marker for EVs. Same procedure for sample preparation was conducted as described in previous Section "*2.2.3.2 Flow cytometry – Characterization of EV surface marker and purity.*" The amount of eFluor 660 fluorescence was quantified using the geometric mean of FL4-A of the vesicle population, which is commensurate with the amount of CD63 per exosome. The fraction of EV incorporation with synthetic lipids were calculated using the normalized geometric mean values, according to the following equation (note that the EV fraction in eEVs = 1 − Synthetic lipid fraction):

$$EV\ fraction\ in\ eEVs = \frac{GM_{eEV}}{GM_{background}} / \frac{GM_{EV}}{GM_{background}} = GM_{eEV}/GM_{EV}$$

Auto-fluorescence or background fluorescence was quantified using samples in the absence of the anti-CD63-eFluor 660 antibody. POPC was used as a stained negative control to compare with native EVs. Isotype igG1 was also pre-tested to get rid of the nonspecific binding concern of antibodies. Note that the above equation will result in values ranging from 0 to 1, where 0 is 100% synthetic lipids and 1 is 100% native EV.

2.2.5. EV and eEV siRNA loading

2.2.5.1. siRNA loading method. siRNA was loaded within EVs and eEVs *via* electroporation using a modified protocol as was previously described (El-Andaloussi et al., 2012b). Briefly, electroporation mixture was prepared in a concentration of 100 µg/ml EV (3×10^{10} particles/ml) or 10^{10} – 10^{11} particles/ml of eEV containing 1 ng/µl siRNA. Note the mass of EVs is represented by the affiliated protein amount as quantified by the Micro BCA assay. Opti-MEM or a hypotonic electroporation buffer (1.15 mM K_2HPO_4; pH 7.2; 25 mM KCl, 21% OptiPrep according to the protocol (Alvarez-Erviti et al., 2011; El-Andaloussi et al., 2012b) were used as the sample solution. Hypotonic buffer was proposed to drive a faster water uptake across vesicle membrane by an imposed osmotic gradient, which facilitates the uptake of genes, resulting in an increase of the transfection efficiency (Golzio et al., 1998; Usaj and Kanduser (2012); Ušaj et al., 2009). Sample volumes of 100 µl were used for electroporation. The siRNA/vesicle mixtures were then transferred to 0.4 cm electroporation cuvettes (#1652088, Biorad) and electroporated using a Bio-Rad Gene Pulser II system, using the following conditions: 400 V, a capacitance of 125 µF, and an exponential pulse induction process. 2 pulses were applied to increase the nucleic acid incorporation or entrapment within the EVs and eEVs, as described previously (Lamichhane et al., 2015). After electroporation, samples were kept on ice for 1 hr to allow for membrane recovery prior to further

experiments.

2.2.5.2. Loaded siRNA content quantification. To quantify the amount of siRNA loaded within EVs/eEVs post-electroporation, the samples were ultracentrifuged at 125,000 g for 70 min. twice to remove free siRNA in solution. The supernatant was discarded after ultracentrifugation and fresh PBS was replenished to each sample as an ultracentrifuge-wash cycle to completely remove loosely bound, free siRNA from EVs/eEVs. As a first step in evaluating the capability of exogenous cargo loading, the actual siRNA amount loaded into the vesicles was quantified. To isolate siRNA from vesicles, a modified TRIzol RNA isolation protocol was used according to previously published literature (Navakanitworakul et al., 2016). Details for the TRIzol RNA isolation are depicted in *Supporting Information*. After siRNA isolation, Quant-iT RiboGreen RNA fluorescent dye (preferentially fluoresces in the presence of RNA (when the nucleic acid is < 500 bp)) was used for the quantification of siRNA, following the manufacturer's instruction. siRNA at varying concentrations were prepared and measured to generate an siRNA calibration curve. To ensure the obtained results represent the loading amount of siRNA, we quantified the amount endogenous RNA within the exosomes, which merely measured at 0.8 ± 0.3 ng of nucleic acid from 10^9 (1E9) exosomes. Compared to our exogenous loading amounts of siRNA (100 ng), it is only ~ 1% of the total amount.

As a control between different lipid-doped systems, a concentration of ~ E10 particles per formulation was carried out under the same vesicle densities for accurate comparison of electroporation efficiency. The loading efficiency (left y-axis) is determined by $\frac{Numbers\ of\ siRNA\ in\ vesicles}{Numbers\ of\ vesicles} \times 100\%$, which represents as siRNA copies per vesicle. The encapsulation efficiency (right y-axis) is determined by $\frac{Mass\ of\ siRNA\ in\ vesicles}{Mass\ of\ the\ feedings\ iRNA} \times 100\%$.

2.2.6. Mitigation of cytotoxicity and aggregation

2.2.6.1. Cell viability assay. The relative metabolic activity of the samples was evaluated using the CellTiter 96® Aqueous Cell Proliferation assay (Promega) (MTS assay) to assess the viability or cytotoxicity levels. Prior to MTS treatment, siRNA-loaded eEVs were incubated with cultured A549 cells at 60 – 70% confluency for 2 hr. After 2 hr incubation, cells were washed to remove excess eEVs and replaced with fresh media for further cell incubation. The MTS assays were conducted after 24 hr of siRNA treatment, following the manufacturer's instruction. Recent animal studies of EVs reported that a dose of 10^9 – 10^{11} EVs (with 1–500 μg siRNA) per 10^5 –10^6 tumor cells (initial cell number) is typically required to achieve therapeutic effects when it is administered every day or every other day (El-Andaloussi et al., 2012b; Haraszti et al., 2018b; Kamerkar et al., 2017; Pi et al., 2018). In regard to our cell viability assay and aggregation studies, we delivered a single dose of 10^9 –10^{10} eEVs with 100–400 ng siRNA per 10^4 cells.

2.2.6.2. Aggregation determined by microscopic image analyses and spectroscopy assays. In addition to NTA and DLS measurements for particle number and size quantification, the degree of aggregation was quantified by a light microscopy imaging method (Gregory (2009)) using Cytation 5 for electroporation-induced aggregates. Particle diameter and number were quantified by Cytation 5's imaging analysis software. To distinguish between background and particles, the bright field intensity was set at 5000 a.u. and the particle size range from 0.5 to 100 μm were set as thresholds. 5 spots per well were imaged and were analyzed. Additionally, spectroscopic assays were employed according to previous studies (Jamaluddin et al., 1987; Lu et al., 2018; Zhang et al., 2015) to determine the turbidity (*i.e.* the absorbance) of the solution. Absorbance spectra were quantified between 230 nm and 998 nm using a spectrometer (Cytation 5). The reading was recorded immediately after loading samples into a 96 well UV transparent plate. The maximum optical density (OD) in the spectrum at 230 nm was used to compare between samples.

2.2.6.3. Mitigation of aggregation and cytotoxicity via electroporation parameters. To assess the electroporation media effects on electroporation-induced aggregation, Opti-MEM, Opti-MEM + EDTA, 50 mM trehalose, and hypotonic electroporation buffer were prepared. In regard to the condition of Opti-MEM + EDTA, 5 mM EDTA was added to the electroporated mixture immediately after electroporation following the protocol from Lamichhane, T. N., et al. who reported similar effects can obtain with EDTA addition either before or after electroporation (Lamichhane et al., 2015). 50 mM trehalose, shown by Hood, J.L. et al. as a membrane stabilizer to ameliorate the electroporation induced-aggregation (Hood et al., 2014), was prepared accordingly. Commonly used hypotonic electroporation buffer (El-Andaloussi et al., 2012b; Tran et al., 2015) was also prepared as mentioned in "2.2.5.1 siRNA loading" section.

2.2.7. Quantification of RNAi knockdown and eEV targetability

2.2.7.1. Quantification of siRNA knockdown in A549 cells. To evaluate the knockdown efficiency of EV-mediated siRNA delivery within the constitutively expressing-GFP-A549 cells over time, GFP fluorescence was measured and quantified using a plate reader (Cytation 5) every day for 12 days (Bishop et al., 2015). To ensure the decrease of green fluorescence intensity is due to the RNA interference of GFP-siRNA in the cells and not caused by the cytotoxicity of the delivery system, each sample type or condition was delivered with scrambled siRNA as a control. The knockdown efficiency was calculated using the below equation:

$$Knockdown\% = 100 \times \left(1 - \frac{(F_{si} - F_{bg})}{F_{osi}} \times \frac{F_{osc}}{(F_{sc} - F_{bg})}\right)$$

where F_{si} is the fluorescence of the well using GFP-siRNA, F_{sc} is the fluorescence of the well using corresponding scrambled siRNA, F_{bg} is the fluorescence background of the media without cells, F_{osi} is the initial fluorescence of the well just prior to delivery for the GFP-siRNA formulations and F_{osc} is the initial fluorescence of the well prior to delivery of the corresponding scrambled siRNA control group. Commercial Lipofectamine® RNAiMax formulation was used as a positive control to compare the knockdown efficiency between samples. The formulation was prepared according to the manufacturer's instruction. Briefly, 0.3 μl of Lipofectamine® RNAiMax was used to deliver 1 pmol of siRNA. The siRNA-Lipofectamine® RNAiMax complexes were mixed in Opti-MEM® media and incubated at room temperature for 10 min. before delivery to the cells. For the *in vitro* siRNA delivery and knockdown assessment, each sample mixture was delivered to the cells for 2 hr. After 2 hr, the sample solutions were replaced by the typical culturing media (with serum) for continual measurements. Area under the curve (knockdown efficiency vs time) was calculated to determine the difference in duration using GraphPad Prism 7 software.

2.2.7.2. Uptake experiments in A549 and CCL-210 cells. 2.5×10^4 cells were seeded on glass coverslips 24 h prior to imaging and quantification. Deep Red Plasma Membrane Stain Cell Mask was used to label EVs/eEVs following the protocol modified from previous literature (Takov et al., 2017). Briefly, EVs/eEVs were incubated with CellMask (1:10000 dilution) in PBS for 5 min. at 37 ^{0}C and then wash-centrifuge three times to remove free Deep Red dyes. Deep Red dye labeled-EVs/eEVs were subsequently added to the cells and incubated for 2 h at 37 ^{0}C. All cells were then fixed with 4% paraformaldehyde and counterstained with 5 μg/ml of Hoechst 33,258 for nuclei visualization. Cell samples were imaged using a confocal microscope (Olympus FV1000). All the images were analyzed with Image J software. To further quantify the uptake efficiency in the cells, cells

were washed with PBS, trypsinized and assayed using a BD Accuri™ C6 Cytometer at a 14 µl/min of flow rate. 10,000 events were collected per sample with triplicates. The signal of Deep Red fluorescence was quantified using the geometric mean of FL4-A of the cell population, which is commensurate with the amount of EV/eEV uptake per cell. To eliminate any cell line-specific difference in the signal background, the following equation was used for calculation:

$$Uptake\ efficiency\ in\ cells = \frac{GM_{EV\ or\ eEV\ in\ A549\ or\ CCL210}}{GM_{untreated\ cells\ (A549\ or\ CCL210)}} / \frac{GM_{eEV\ in\ A549}}{GM_{untreated\ A549}}$$

Untreated A549 and CCL-210 cells were measured as a negative control. The uptake of POPC-EV in the absence of Deep Red dye staining in A549 and CCL-210 was also examined to confirm no autofluorescence interference from the vesicles. It is important to note that the excessive lipophilic dye staining with exosomes may cause non-specific binding to the cell membranes, resulting in false-positive signals or the change of exosome uptake pathways (Dominkuš et al., 2018; Simonsen, 2019). Our (dye only) control which was similarly centrifuged serially and assayed via flow cytometry indicated the background fluorescence was only 1.4 ± 0.3% and 4.2 ± 0.9% of the A549 and CCL210 cells' samples, respectively.

2.2.8. Statistics

Data are presented as the mean ± the standard deviation (SD). All experiments were conducted with triplicates (Exception are indicated specifically as below). Statistical data analyses were performed using GraphPad Prism 7 software. The α value was set at 0.05, where *, **, ***, **** represent *p*-values < 0.05, < 0.01, < 0.001, and < 0.0001 respectively. The following statistical tests were conducted for each figure: ***Unpaired, two-tailed Student's t-test:*** Fig. 1B; 2A/B; Fig. S10; S15A and B; S17. ***One-way ANOVA, followed by Dunnett's multiple comparison test (post-hoc):*** Fig. 2C (compared to EV); Fig. 2E (compared to EV in water and PBS, respectively); Fig. 3A (compared to EV); Fig. 3D (compared to EV; n = 2 for negative control group); Fig. 4 (compared to EV); Fig. 6A (compared to Opti-MEM group); Fig. S14 (compared to untreated cells); Fig. 7B and D (compared to EV). ***One-way ANOVA, followed by Tukey's multiple comparison test (post-hoc):*** Fig. 2D; Fig.S4; Fig. 3A (to compare each lipid-doped eEVs at varying ratio, no statistical difference in the results); Fig. 5A (technical replicates of n = 3); Fig. 6B; Fig. S7; S12C; S17A and B; Figs. 7C; 8B.

3. Results and discussion

Lipid hybridized EVs, called engineered extracellular vesicles (eEVs), were prepared by sonication and extrusion method, as summarized in Scheme 1. To manufacture eEVs, EVs were first collected and characterized. In this work, we obtained batches of EVs from A549 and 3 T3 cells using a gold standard protocol (Xu et al., 2016), involving serial centrifugation and ultracentrifugation to isolate EVs, specifically exosomes, from culturing media. However, it is reported that EVs isolated from ultracentrifugation often produces exosomes containing impurities of microvesicles or impurities of protein aggregates adsorbed on the isolated vesicles (Tran et al., 2015). Due to the possibility of co-presence of microvesicles and exosomes within our population of vesicles, we named our system "extracellular vesicles" (EVs) to avoid any confusion or argument.

3.1. Physicochemical quantification of EVs from cells

The isolated EV populations were initially characterized by transmission electron microscope (TEM), nanoparticle tracking analysis (NTA), total protein content and flow cytometry. Representative size distribution profiles of EVs revealed by NTA are shown in Fig. 1A. Average particle diameters of 124.3 ± 14.7 nm and 90.1 ± 18.6 nm were obtained for EVs derived from 3 T3 (3 T3 EVs) and A549 cells (A549 EVs), respectively. The EVs from both cell types had uniform and narrow size distributions. No larger particles above 500 nm were observed. TEM morphology (inlet image of Fig. 1A **and Fig. S1)** demonstrated spherical shape of the vesicles. In terms of the production yield, we obtained 3 T3 EVs on the order of $(1.97 \pm 0.37) \times 10^9$ particles from 10^7 cells, namely, 197 ± 37 EVs per cell; whereas a higher amount of EVs were released per cell from A549 cells, on the order of $(4.80 \pm 0.23) \times 10^9$ particles from 10^7 cells (480 ± 23 EVs per cell), as shown in Fig. 1B **(left y-axis)**. On the other hand, representative protein amounts of EVs quantified by Micro BCA assay are shown in Fig. 1B **(right y-axis)**. Amounts of 0.20 ± 0.08 µg protein and 0.08 ± 0.05 µg protein within 10^8 EV particles were quantified in 3 T3 EVs and A549 EVs, respectively. Our characterizations of EVs are similar to the production yields of U937 (human monocytic cells)- and HEK293T (human embryonic kidney cells)-derived exosomes reported from previous studies (Jang et al., 2013; Pi et al., 2018). As a model system for gene delivery, the yields of EV production from parental sources and the selectivity to the cells of interest need to be considered. Our data demonstrated A549 cells had a 2.4-fold higher (***$p < 0.001$) production yield of EVs compared to the EV yields of 3 T3 cells. We chose A549 cell as the source of EVs to generate batches of eEVs because of their relatively higher production yield and potential targetability of tumor derived-extracellular vesicles to tumor cells (Christianson et al., 2013; Rana et al., 2012). Although human mesenchymal stem cells (hMSCs)-derived EVs are well-known as an efficient mass producer of EVs (Yeo et al., 2013) (~2100 ± 300 released hMSC EVs/cell, ~5-folds higher than A549 cells, based on our data), due to the limited expansion of hMSC culture (Turinetto et al., 2016) and favorable doubling time of A549 cells (greater than 50 h for hMSCs (Jin et al., 2013) whereas 22 h for A549), we opted to use A549 cells, for the purpose of demonstrating the development of scalable eEVs. Isolated A549 EVs were then analyzed by flow cytometry for the presence of specific markers. As shown in Fig. 1C, fluorochrome-labeled anti-CD63 binding EVs and nonfluorescent isotype control showed discernible populations in the gate FL1 versus FL4 (anti-CD63-eFluor 660). Results showed CD63 is highly enriched in the isolated EV samples. 87.4% of the isolated samples were positive for the exosomal marker CD63 (Fig. 1D). Therefore, we expected the majority of our EVs to be exosomes (CD63 +), as opposed to microvesicles where CD63 was typically not detected (CD63-) (Kanada et al. (2015)).

3.2. Physicochemical quantification of eEVs from cells

To generate eEVs, the isolated EVs were then fused with pre-hydrated lipids using a sonication and serial extrusion procedure. We investigated whether different charges of lipids could be incorporated to native/naïve cell derived EVs. A library of lipids (DOTAP, POPC, DPPC and POPG) was therefore prepared for membrane hybridization. The structures of these lipids are as shown in **Fig. S2**. After producing lipid-doped eEVs, we characterized the morphology, size, mass production and zeta potential of eEVs. Fig. 2A and B show the size distribution profiles of pre-hydrated POPC liposomes alone and POPC-doped eEVs, respectively: 138.8 ± 9.1 nm and 126.3 ± 4.0 nm (***$p < 0.001$; statistically significant). The inlaid TEM images of Fig. 2A and B depict the morphology of pre-hydrated POPC liposomes alone and intact structure of POPC-doped eEVs. While heterogeneous size of pre-hydrated liposomes was shown in Fig. 2A, a lamellar structure and uniform size of vesicles approximately 100 nm were demonstrated in Fig. 2B for eEVs. The TEM morphology confirmed the vesicle structure was not impaired by the sonication-extrusion method, indicating the extrusion apparatus is a suitable method for fabricating lipid-hybridized eEVs. We further characterized a variety of lipid-doped eEVs at varying extruded ratios (from 1:1 to 9:1 of lipid to EV mixing ratio) by performing the same sonication-extrusion processes, as shown in Fig. 2C. As expected, the average diameters of eEVs measured by NTA indicated that eEV formulations are much smaller than 200 nm size, thus these formulations would likely be able to take advantage of

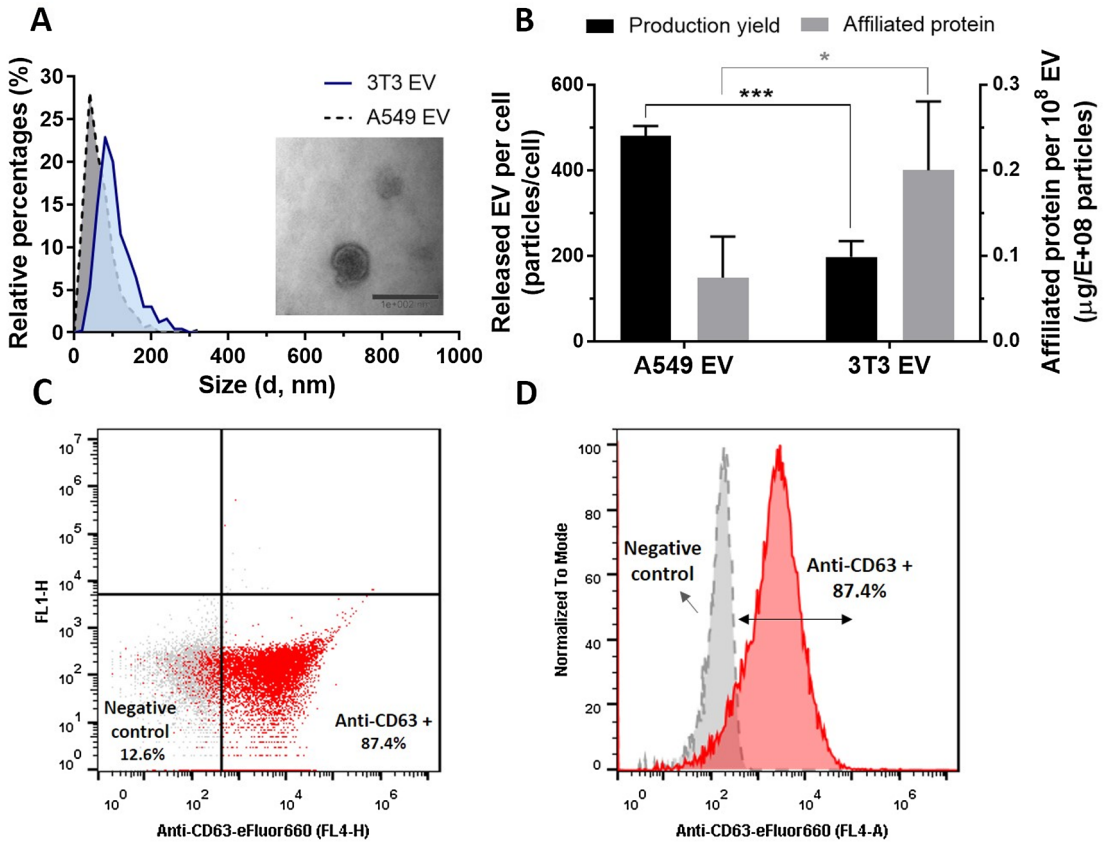

Fig. 1. Characterization of extracellular vesicles (EVs) after ultracentrifugation. (A) reports the relative size (diameter) distribution profiles for A549 (dashed line, gray peak) and 3 T3 cell (solid line, blue peak) -derived EVs. A transmission electron microscope (TEM) image inlaid within (A) showed the spherical structure of EVs (3 T3 EV; scale bar: 200 nm). **(B)**'s left y-axis reports the production yield of EVs secreted by A549 and 3 T3 cells. Affiliated protein per EV (Micro BCA assay) is reported on the right y-axis of (B). **(C, D)** Flow cytometric analysis of EVs stained with fluorescent labelled antibodies targeting CD63. **(C)** reports a scatter plot of A549 cell-derived EV (red dots on bottom right of (C)) and the negative isotype control (gray dots, bottom left box of (C)). **(D)** reports a histogram of $CD63^+$ A549 EVs stained with anti-CD63-eFluor 660 (solid line, red peak) and negative isotype control (dashed line, gray peak). (* and *** represent p-values < 0.05 and < 0.001, respectively). (For interpretation of the references to colour in this figure legend, the reader is referred to the web version of this article.)

the enhanced permeability and retention effect (Sun et al., 2013). Among each individual lipid-doped eEVs, no statistical difference on the particle size for eEVs at varying extruded ratio was observed.

Several studies have endeavored to develop scalable techniques at the stages of EV generation and purification, such as: using a two compartment culture (Integra CELLine) (Mitchell et al., 2008); a microcarrier-based 3D culture (Haraszti et al., 2018b); a hollow-fiber culture system (Watson et al., 2016); and a tangential flow filtration system for purification (Haraszti et al., 2018b). Among these studies, a 7-fold to 40-fold increase in the production yield of EVs was achieved. In this study, instead of scaling up the production of EVs from the cells, we attempted to mass produce the vesicles after EV isolation. By evaluating the quantity of eEVs using NTA measurements, we observed a constantly higher production yields over various conditions (*i.e.* different lipid-doped eEVs and varying lipid:EV ratios) obtained by our sonication-extrusion technique compared to native EV production yields, as shown in Fig. 2D. On average, there was a 6-fold (for DPPC-EV 1:1 samples) to 43-fold (for DOTAP-EV 9:1 samples) increase on the overall amount of particle number upon the sonication-extrusion processes (Fig. 2D). While DOTAP-EV showed an average of 20-fold further increase of particle yields, POPC-EV, DPPC-EV and POPG-EV showed similar 10-fold increase values. Initial particle number of different lipid types in same molar concentration were also quantified in **Fig. S3**. No statistical difference of particle number was shown among different types of lipids. These results indicated that the increase of particle number after sonication-extrusion technique most likely depends on the physical–chemical properties of lipids (*i.e.*, charge), instead of the initial particle numbers of lipids. Overall, the production yields of eEVs generated post-EV isolation were about ~ 8-fold higher than the number of EVs obtained from hMSCs using typical cell generation method, according to the results of hMSC EV from previous literature (Haraszti et al., 2018b; Yeo et al., 2013).

While others have integrated other synthetic materials (*i.e. via* freeze-thaw methods and PEG-induction methods) to already-isolated-EVs, such as liposomes and have proposed such systems as potential drug delivery carriers (Antimisiaris et al., 2017), our system highlights the ability to mass produce the number of vesicles, as opposed to multi-lamellar/hybridized EVs (Piffoux et al., 2018; Sato et al., 2016). Furthermore, our data of different lipid-doped eEVs demonstrate that the mass production can be tuned by the incorporation of EVs with cationic, anionic, and zwitterionic lipid chains.

To evaluate the difference of lipid: EV mixture before and after the sonication-extrusion processes, zeta potentials of the vesicles were measured, as shown in **Fig. S4**. The data showed the sonication-extrusion processes significantly alters the zeta potential of the samples in comparison to the samples of physical mixture (*$^{**}p < 0.01$ and $^{***}p < 0.001$ for POPC-EV 4:1, 1:1 and 9:1 group, respectively*). The zeta potentials of the eEVs at varying extruded ratio were also statistically different (*$^{****}p < 0.0001$*) compared to the native exosomal membrane (**Fig. S4**). We further characterized the zeta potentials of EV and eEVs measured in PBS and water, as shown in Fig. 2E. It is known that phospholipids, such as cholesterol, phosphoglycerides, ceramides and saturated fatty acids, are rich within EV membranes (Ren et al., 2016). The presence of saturated phospholipids and the anionic surface charge

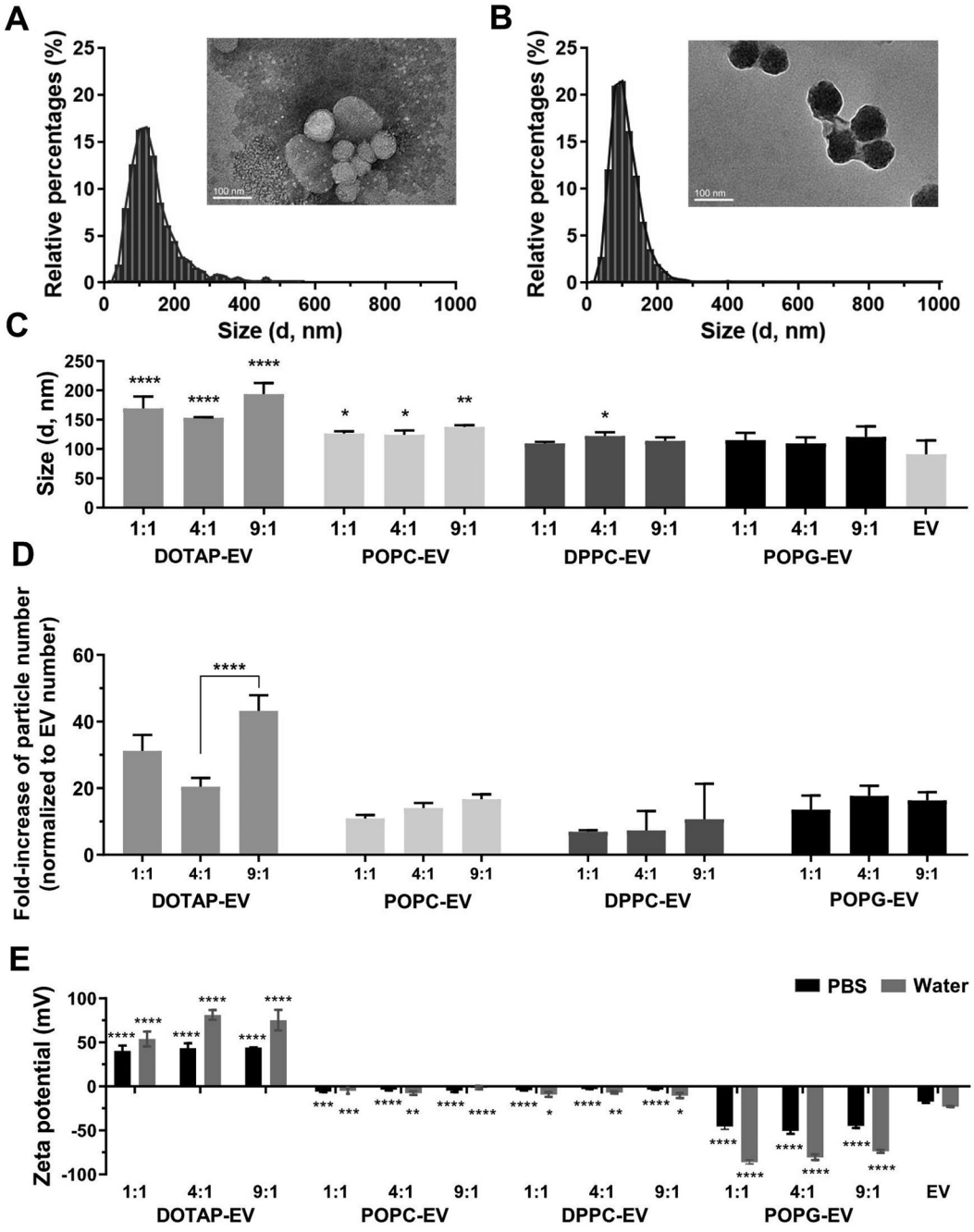

Fig. 2. Morphology, size, quantification of mass production and zeta potential measurement of engineered extracellular vesicles (eEVs). The size distribution profiles and morphology of vesicles for hydrated lipids POPC **(A)** and engineered EVs: POPC-EV **(B)** were measured by NTA and TEM. Scale bar represents 100 nm. The mean diameters **(C)** of different lipid-doped eEVs were determined by NTA measurement. Fold increase in particle number **(D)** was quantified by normalizing the concentration of eEVs after extrusion processes to the concentration of original native EV concentration before extrusion processes. Zeta potential values measured in water and PBS are reported in **(E)**. (*, **, ***, ****, represent p-values < 0.05, < 0.01, < 0.001, and < 0.0001, respectively).

help contributed to the high stability of EVs (Ren et al., 2016). Therefore, relatively negative zeta potentials of EVs were obtained with –22.9 ± 0.6 and −17.3 ± 1.4 mV in water and PBS, respectively. Compared to the zeta potentials of samples measured in pure water, zeta potentials in PBS were closer to neutral (0 mV). These results can be attributed to the charge shielding effects by salt ions present. These data are similar to the zeta potential of EVs generated from the neuroblastoma cell lines reported previously (Marimpietri et al., 2013), which ranged from −14.8 ± 1.6 to −12.0 ± 0.2 mV in a PBS solution. On the other hand, the zeta potentials of eEVs were found to correspond to the charge of extruded lipids. DOTAP-EV, POPC-EV and DPPC-EV, and POPG-EV showed positive, neutral, and negative charge, respectively (Fig. 2E), indicating the zeta potentials of eEVs can be tuned by hybridizing EVs with different charge types of synthetic lipids. Taken together, our data demonstrate the sonication-extrusion processes significantly alters the zeta potential of eEVs, suggesting that there were substantial alterations of the lipid content within the eEVs.

3.3. Quantifying native EV fraction within eEVs for validating membrane incorporation

In the current study, we first chose lipid (SPV) and protein (Micro BCA) assays that are widely used in the EV field to determine membrane incorporation within the vesicles. Before determining the protein

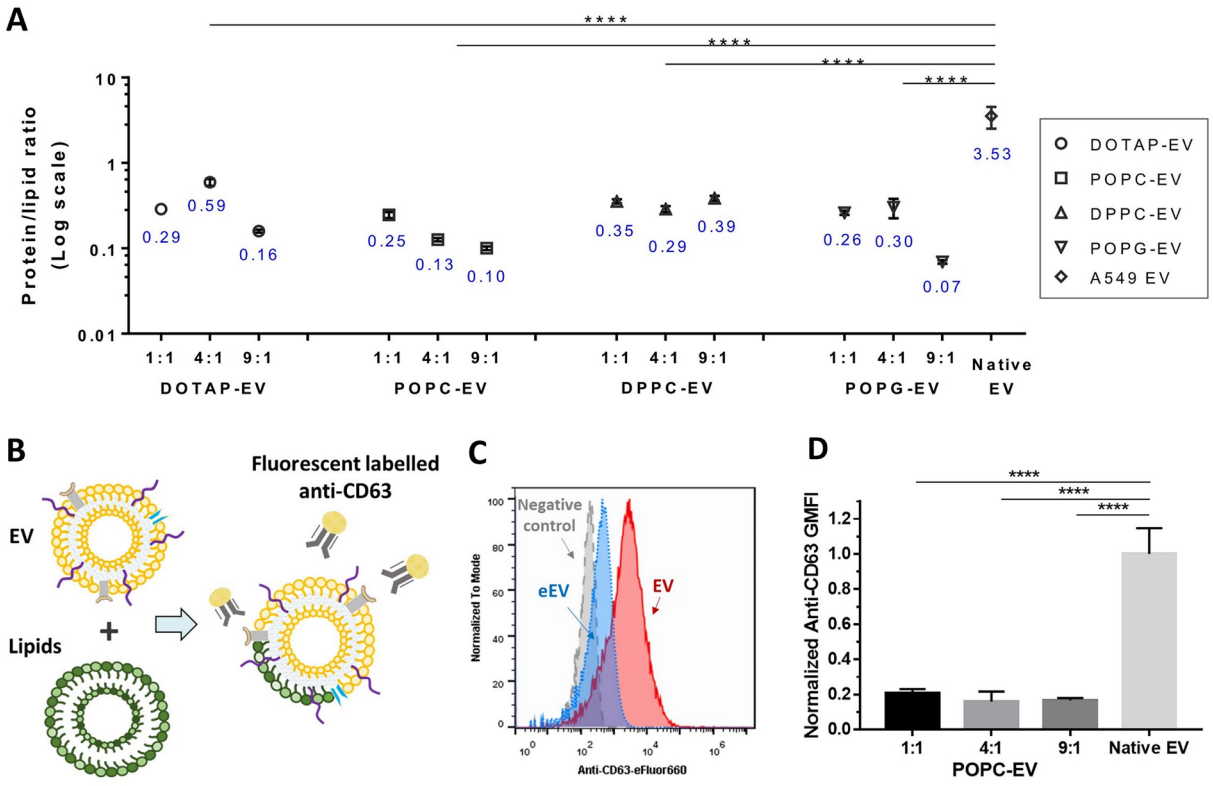

Fig. 3. Assessment of membrane incorporation of engineered extracellular vesicles (eEVs) via protein: lipid ratio quantification and FACS analysis. The protein: lipid ratios within the membrane of different lipid-doped eEVs were quantified in **(A)**. An illustration of membrane incorporation validation within eEV entities using anti-CD63 detection via flow cytometry is shown in **(B)**. Flow cytometry histograms **(C)** of: A549 EVs stained with anti-CD63-eFluor 660 (solid line, red peak); eEV stained with anti-CD63-eFluor 660 (dotted line, blue peak); and a stained isotype (dashed line, gray peak), functioning as a negative control. The normalized anti-CD63 geometric mean fluorescence intensities (GMFIs) are shown in **(D)** and quantify the fusion ratio of synthetic lipids doped within EVs, thereby forming eEVs (0–1 represents 0%- 100% native EV). (**** represents p-values < 0.0001). (For interpretation of the references to colour in this figure legend, the reader is referred to the web version of this article.)

to lipid ratios in EVs/eEVs, preliminary tests of individual lipid species were measured as references, which showed good linearity of absorbance in the range of 0–2 μg/μl lipid concentration using SPV assay (Fig. S5). In parallel to the lipid quantification, pure lipid solutions were also tested for their assay interference with the protein determination (Fig. S6). No substantial interference on the protein Micro BCA assay by lipids was observed, as the data did not result in strong colorimetric reactions. We then evaluated the protein quantities between the physical mixtures of EV: lipid and the eEVs following sonication-extrusion processes. Fig. S7 evidences a statistically significant change (****$p < 0.0001$) of protein quantities in the lipid-EV mixture before (physical mixture in the absence of sonication-extrusion processes) and after sonication-extrusion processes (lipid-doped eEVs). To further determine the fusion efficiency of exosomal membrane in eEVs, we quantified the protein to lipid ratio, which has been proven to be a good quality control parameter of EVs previously (Osteikoetxea et al., 2015). Fig. 3A presents the calculated protein to lipid ratios of EVs/eEVs. The protein to lipid ratios of eEVs (0.069 ± 0.004 to 0.594 ± 0.055) significantly (****$p < 0.0001$) dropped compared to the protein to lipid ratio of EVs (3.529 ± 1.015). These results demonstrate the exogenous synthetic lipids were doped within EVs. With the addition of lipids to EVs, the overall percentage of lipids within the membrane increases, results in the dropping of the protein to lipid ratios within eEVs. In comparison to the pure lipid solutions (Fig. S6), our results showed a 5-

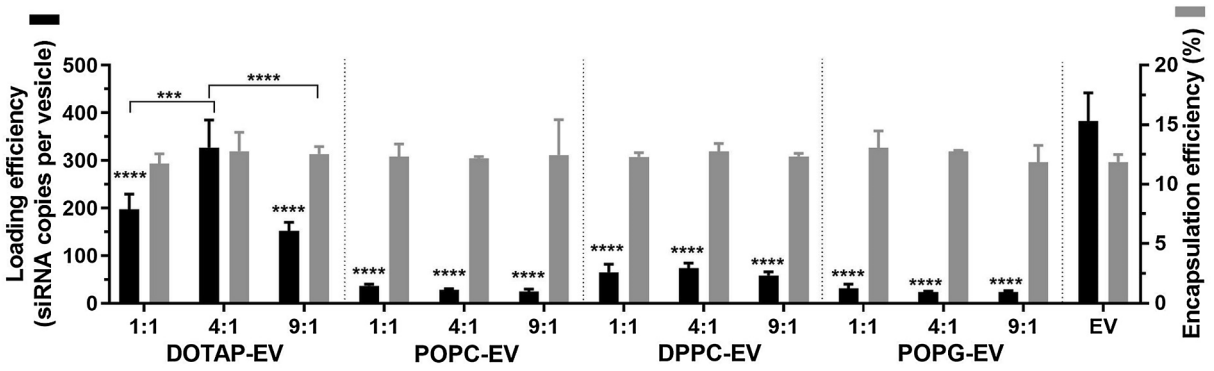

Fig. 4. Exogenous loading of siRNA *via* electroporation system. Left y-axis reports siRNA loading efficiency (black) and right y-axis reports encapsulation efficiency (gray). (*** and **** represent p-values < 0.001 and < 0.0001, respectively).

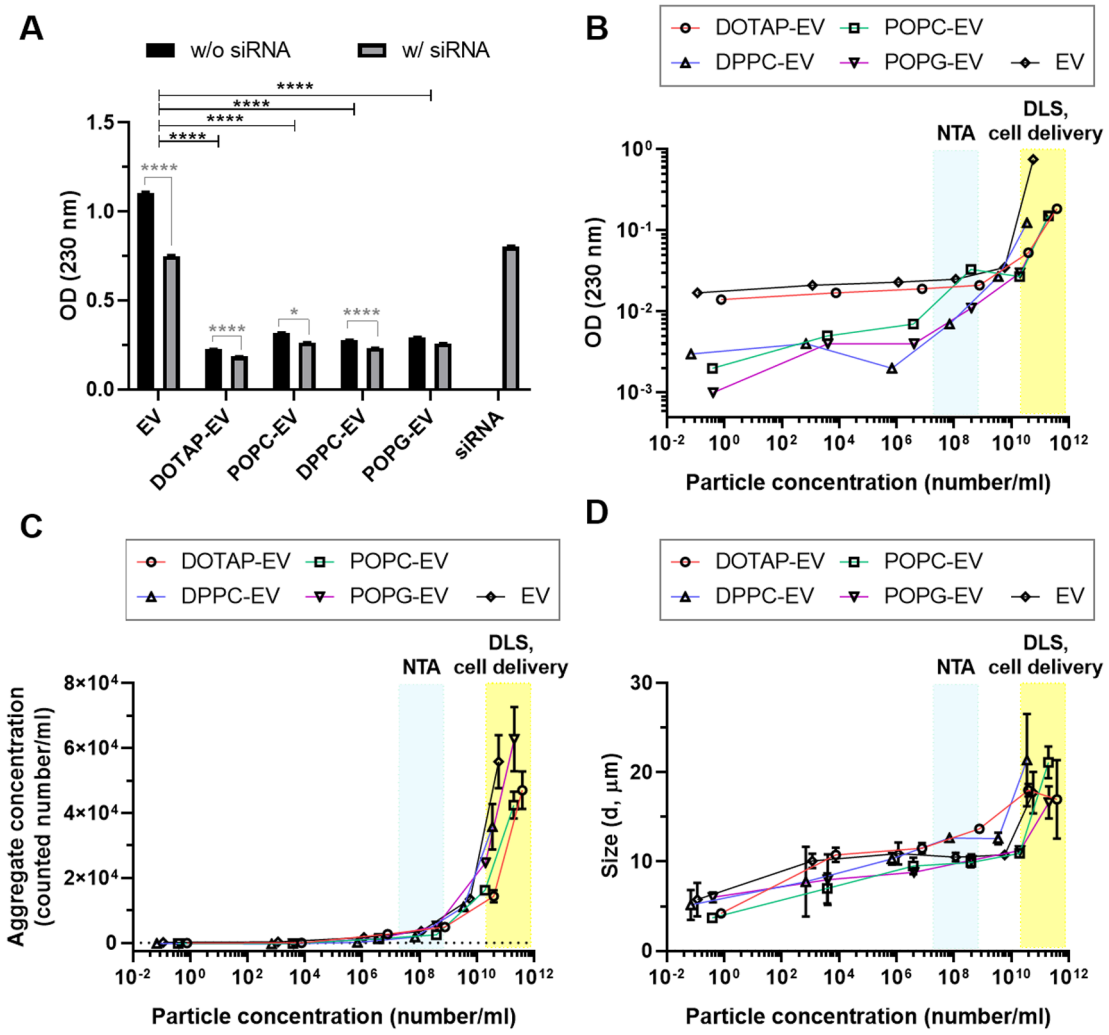

Fig. 5. Characterization of aggregation post-electroporation by spectroscopic assays and microscopy image analysis. (A) shows the turbidity (OD: 230 nm) for EV, eEVs and siRNA conditions in the absence of siRNA (w/o siRNA, meaning only vesicles in the solution) or in the presence of siRNA (vesicle + siRNA) during electroporation. The absorbance values in y-axis have the background values (Opti-MEM media/pre-electroporated samples) subtracted. **(B)** is a log–log plot of turbidity (OD: 230 nm) versus vesicle concentration after electroporation. **(C, D)** are semi-log plots of aggregate counts per ml and aggregate size (diameter) versus vesicle concentration after electroporation. Data were determined by microscopy image analysis. **(B, C, D)** The blue regions are the concentrations suitable for NTA quantification, whereas the yellow regions are the concentrations suitable for cell delivery and DLS quantification. (For interpretation of the references to colour in this figure legend, the reader is referred to the web version of this article.)

fold (DPPC-EV 4:1/DPPC lipid = 0.29/0.057) to 42-fold (DOTAP-EV 4:1/DOTAP lipid = 0.59/0.014) of protein to lipid ratio change within eEVs upon the membrane extrusion procedure. Note that the protein to lipid ratio only slightly changed at varying extruded ratio, as no statistical difference was observed (Fig. 3A). Similar trend of the protein to lipid ratio within eEVs was obtained while using the EVs from different cell sources (3 T3 EV and A549 EV) (**Fig. S8**), indicating this technique for membrane incorporation can be applied to EVs derived from different parental cells.

To further confirm the membrane fusion of exogenous synthetic lipids within the EVs, as opposed to synthetic lipids and EVs being physically mixed, flow cytometry was used to detect the fluorescence of each entity (Fig. 3B). The histogram plot of anti-CD63 fluorescence is shown in Fig. 3C. Normalized geometric means of fluorescence confirmed the percentage of membrane incorporation in POPC-EV (1:1, 4:1, 9:1) samples as a fraction ratio of 0.16 to 0.21 (Fig. 3D), meaning the eEVs having 16–21% native EV membranes within them. Similarly, no statistical difference was observed at varying extruded ratio for eEVs. The results of our flow cytometry-based assays and the membrane protein/lipid assays corroborate each other, in that both illustrate our sonication-extrusion process fused a fraction of each of the synthetic lipids within the EVs. The histogram plot of anti-CD63 fluorescence in flow cytometry demonstrated individual eEVs present higher CD63 + levels compared to the control group of liposome-POPC as background fluorescence and lower levels compared to native/naïve EVs, suggesting the successful fusion of exosomes with lipids. These data demonstrate our method of generating EVs can increase the yield of particles post-EV isolation while retaining native protein (*i.e.* CD63) within each entity.

It is interesting that we did not observe statistical differences of eEVs at varying extruded ratios in both protein/lipid assays and flow cytometry experiments, indicating we were likely at a point of saturation, in terms of the amount of synthetic lipid that could be incorporated into the membrane. These results are different from the lipid-hybridized EVs triggered by PEG-induced fusion reported from literature (Piffoux et al., 2018), who showed that 9% to 56% of lipids could be incorporated by varying EV:lipid ratios. This discrepancy between the two methods could likely be attributed to the difference of lamellarity and localization of lipids within the EVs. While 30–40% of multi-lamellar vesicles tend to form using PEG-induced lipid:EV fusion

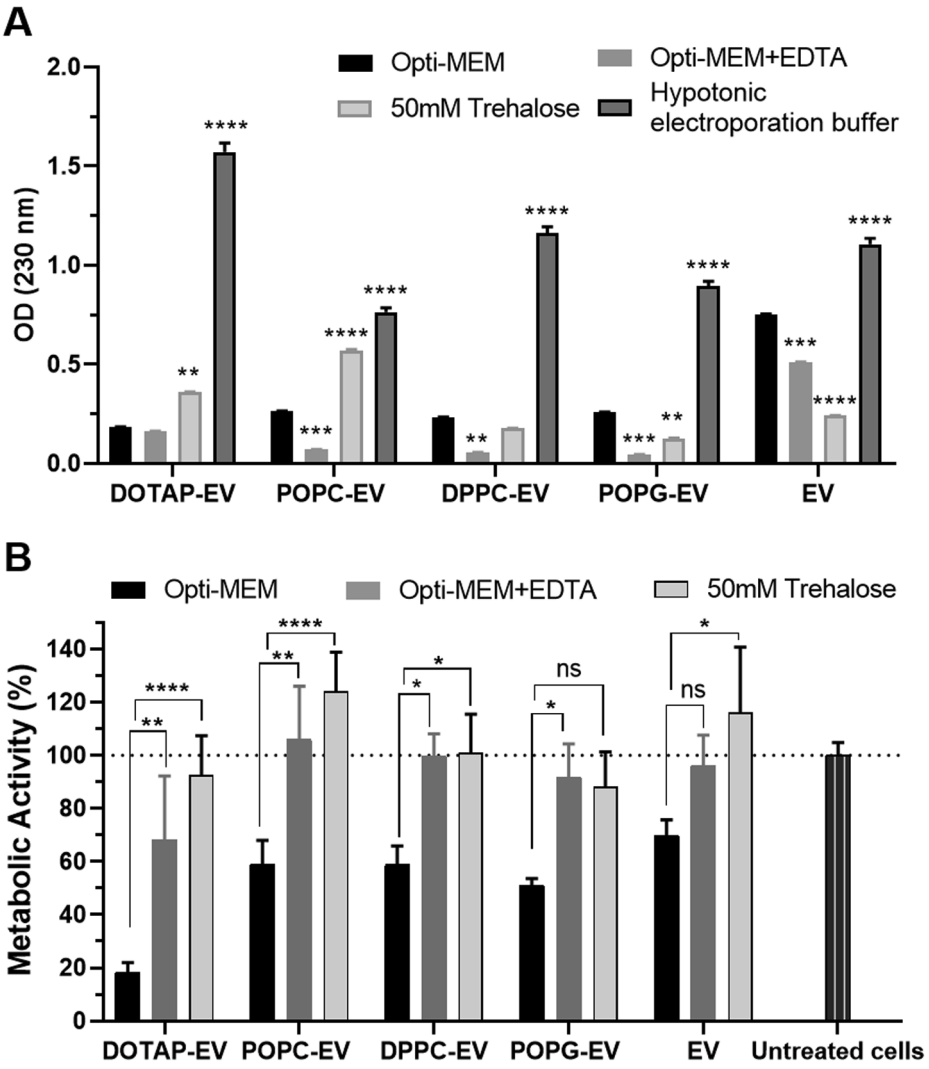

Fig. 6. Effects of electroporation media on the formation of aggregates (A) and cell viability (B). Note: The cell viability assay was not conducted for eEVs in hypotonic electroporation buffer due to the excessively high level of aggregation.

(Piffoux et al., 2018), additional studies for lipid-doped eEVs using sonication-extrusion processes would need to be conducted to suggest a percentage, which we plan to do in the near future.

3.4. EV and eEV siRNA loading

The capability of EVs for efficient drug loading without drastic physicochemical modification of the native vesicles is one of the major and practical obstacles in the clinic. After generation of lipid-fused eEVs, we attempted to encapsulate exogenous siRNA into the vesicles. As a first step in evaluating the efficacy, we assessed the changes of physicochemical properties following electroporation. Fig. S9**A** reveals intact and round shaped morphology of eEVs post-siRNA loading *via* electroporation. Occasionally, we found the vesicles appeared fused or aggregated after electroporation (Fig. S9**B**). No obvious alternations on the vesicle size of the samples after electroporation were observed by NTA measurement at the concentration of $\sim 10^8$ particles per ml (Fig. S10**A**). However, there was a statistically significant change ($^*p < 0.05$) on the z-average diameters of the vesicles post-electroporation, as measured by DLS at concentration of $\sim 10^{11}$ particles per ml (Fig. S10**B**). Fig. S10**C** demonstrates the zeta potentials of eEVs after electroporation significantly decreased ($^{**}p < 0.01$) from -4.9 ± 3.5 mV to -28.0 ± 3.5 mV. Possible reasons for the differences between the results from the two instruments could be that DLS is biased towards large particles or aggregation occurs at higher concentration of the samples required for DLS measurement ($\sim 10^{11}$ particles/ml) compared to the sample concentrations required for NTA measurements ($\sim 10^8$ particles/ml).

We furthered assessed the actual siRNA amount loaded into the vesicles. Prior to siRNA purification and quantification procedures, free unbound siRNAs in the sample mixture were removed by centrifugation and wash. By repeating these steps, our data showed only $1.2 \pm 0.2\%$ of free siRNA retained in the pellet after centrifugation, validating the efficacy of removing free unbound siRNA. To evaluate siRNA loading efficiency via electroporation, we first demonstrated the buffer used for electroporation (hypotonic buffer vs isotonic Opti-MEM) does not substantially affect siRNA loading efficiency (Fig. S11; no statistical difference) but does affect the retention of siRNA within the vesicles (Fig. S12). The gel images and semi-quantified results in Fig. S12 demonstrated the siRNA was confined in the sample well with the electroporation condition using Opti-MEM media, resulting in a lower siRNA migration amounts than the samples using hypotonic electroporation buffer. In other word, using Opti-MEM media, siRNA was retained and bound within the vesicles. Based on these findings, Opti-MEM was used for all further evaluations.

Subsequently, we quantified the loading efficiency (Fig. 4, **left y-axis**) and encapsulation efficiency (Fig. 4, **right y-axis**) of each lipid-doped eEV system. We demonstrated exogenous siRNA can be loaded

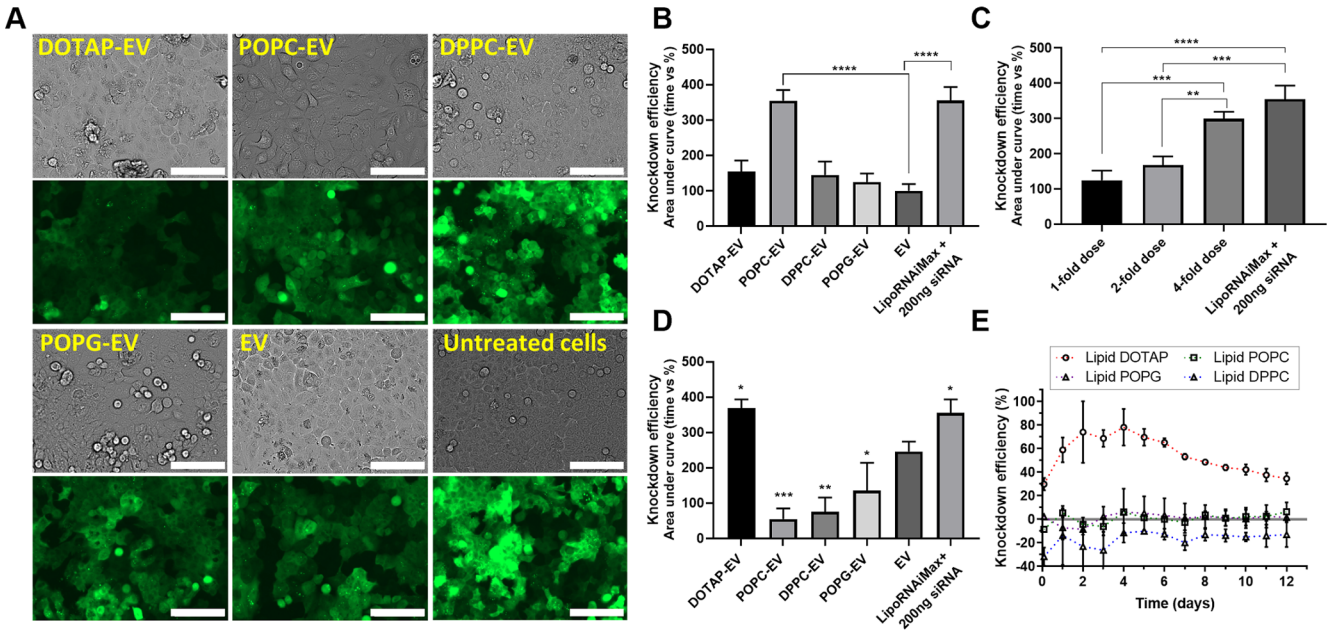

Fig. 7. RNA interference knockdown of eEVs in lung tumor cells (A549). (A) shows fluorescence images of delivered anti-GFP siRNA with eEVs to A549 cells at 3 days post-transfection. scale bar: 100 μm. **(B, C, and D)** show the statistical analysis of overall knockdown efficiency of eEVs. **(B)** shows the effects of EV and eEVs in Opti-MEM + EDTA. **(C)** shows the effects of delivered dosages. POPG-EV in 100 μl Opti-MEM: 1-fold, 2-fold, and 4-fold are (10^{11} particles/ml, 1 ng/μl siRNA), ($2x10^{11}$ particles/ml, 2 ng/μl siRNA) and ($4x10^{11}$ particles/ml, 4 ng/μl siRNA), respectively. **(D)** shows the effects of EV and in 50 mM trehalose. **(E)** shows the knockdown curves over time of lipid-siRNA complexes following electroporation. Same molecule concentration (2.5 μl of 2.5 mM) of lipids as the final amounts used for eEV-siRNA delivery was prepared.

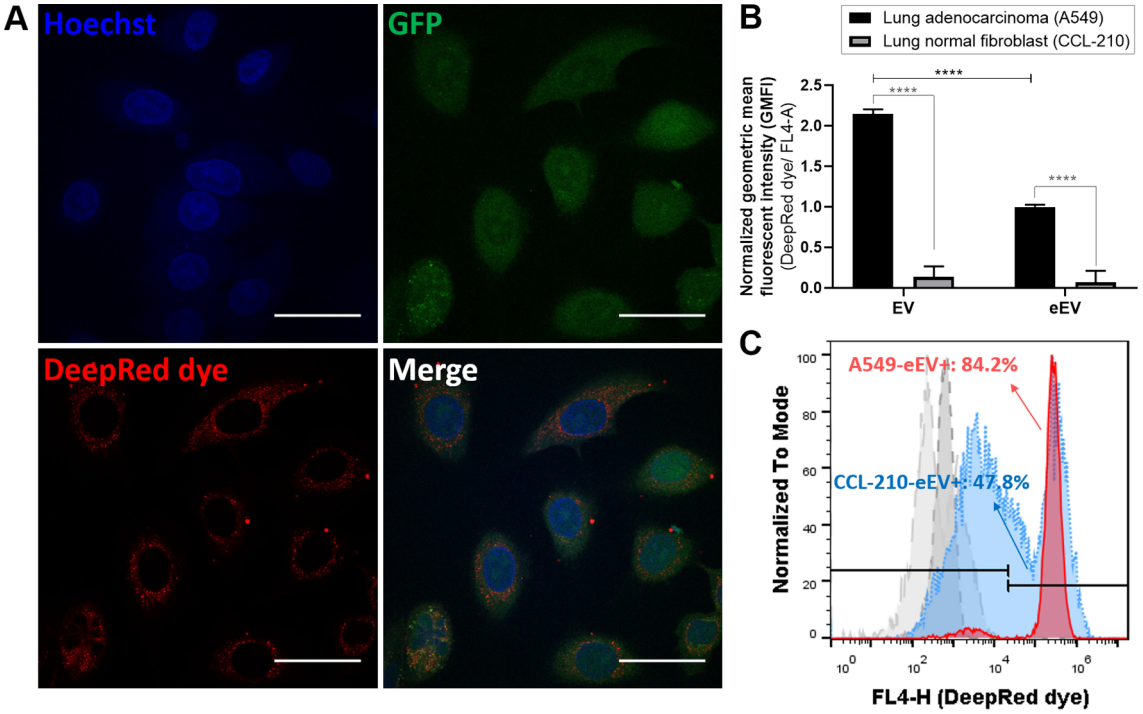

Fig. 8. Visualization and quantification of eEV uptake to lung adenocarcinoma (A549) and lung normal fibroblast (CCL-210). (A) Confocal microscopy images of eEV (POPC-EV) incubated with A549 cells for 2 h. Red indicates the DeepRed®dye for eEV membrane staining; Blue indicates Hoechst 33,342 nuclei staining; Green represents the GFP expression in cell cytoplasm of A549 cells; Scale bar: 30 μm; **(B)** Normalized geometric mean fluorescence intensities (GMFI) from flow cytometry analysis to compare the cellular uptake efficiency of eEVs in A549 and CCL-210. 10^{11} particles of POPC-EV was used as representative of eEVs; same amounts of EVs (10^{11} particles) were delivered to the cells to compare the uptake efficiency. **(C)** Flow cytometry histograms (FL4-H) of eEVs uptake by A549 and CCL-210 cells; Grey dashed peak: Untreated A549 cells; Grey long-dashed peak: Untreated CCL-210; Blue dotted peak: eEV uptake in CCL-210; Red solid peak: eEV uptake in A549. (For interpretation of the references to colour in this figure legend, the reader is referred to the web version of this article.)

into eEVs and the loading efficiency is dependent on the hybridized lipid types. The loading efficiency results showed we were able to obtain 23 – 327 copies of siRNA per vesicle. Particularly, DOTAP-EVs showed highest loading efficiency, which was at least 8-fold higher than other lipid-extruded eEV systems. Moreover, the loading efficiency of cationic lipid-doped eEVs is comparable to the loading efficiency of unmodified, native EVs (Fig. 4; no statistical difference). Taken together, zwitterionic eEVs (POPC-EV and DPPC-EV) and anionic eEVs (POPG-EV) exhibit generally comparable loading profiles (no significant difference between each other).

Consistent with the previous findings by the Wood's research group (Alvarez-Erviti et al., 2011; El-Andaloussi et al., 2012a), we obtained similar electroporation efficiencies (~15 – 20% of siRNA could be encapsulated in EVs/eEVs by electroporation). Overall, in our results, electroporation seems to be a robust method for cargo loading within our eEVs, albeit aggregation issues could be a concern for cell studies. To explore the potential electroporation-caused aggregation of vesicles, we will now further discuss the sub-micron aggregates and their effects on cells.

3.5. Mitigation of eEV aggregation and its effects on cytotoxicity

In the present study, we established a more stable (in comparison to what was initially commercially procured), and higher GFP-expressing tumor cell model (A549) for *in vitro* cell studies. The detailed methods and results are depicted in ***Supporting Information*** (**Fig. S13**). This GFP model allows us to easily visualize and quantify the delivery of anti-GFP siRNA, and the resulting knockdown of the GFP using fluorescence microscopy, fluorescence plate readers, and flow cytometry. In this section, we first conducted the cell viability (MTS) assay to evaluate if there is any cytotoxicity issue with siRNA loaded EV/eEV (10^{10}-10^{11} vesicles/ml) post-electroporation (**Fig. S13**). Unexpectedly, independent of the lipid-doped eEV used, the viability was lower than 70%. Although in the previous section DOTAP-EVs were associated with higher siRNA loading efficiency, here it resulted in the highest toxicity, ranging from 18.2 ± 3.8% to 56.5 ± 3.9% at varying lipid:EV ratio (**Fig. S14**). The cytotoxicity of DOTAP-EV could potentially be attributed to the charge of lipids, which has been shown to be toxic to the cells at high concentrations, although it is commonly used as a transfection agent (Lv et al., 2006). In addition to the charge effects from the lipids, we hypothesized these cytotoxic results could likely be attributed to particle aggregation and sedimentation of the eEV-siRNA delivery system, as was seen in the brightfield images (**Fig. S14**), note the precipitation of eEV within the bright field image of the engineered DOTAP-EV and DPPC-EV formulation. It is currently believed that the electric pulses from electroporation may cause undesirable metal ions to release from the electrodes and subsequently affect the lipid oxidation and the solubility of a variety of biomolecules [71]. In order to investigate whether the toxicity was due to the electroporation process or not, **Fig. S15** quantifies the cytotoxicity of eEVs with siRNA mixture in the absence of electroporation, that the viability remained high (~80 – 125%) and was relatively independent of particle concentration. In other words, there were no obvious signs of toxicity observed in A549 cells while increasing the eEV concentrations from $(0.13 – 1.08) \times 10^{11}$ and $(0.95 – 15.72) \times 10^{11}$ particle/ml for the engineered DOTAP-EV and POPG-EV formulations, respectively. However, there was a significant reduction of cell viability for both eEV-siRNA mixture assessed post-electroporation: DOTAP-EV (post-electroporation) decreased 7-fold to only 18% viability (***$p < 0.001$) and POPG-EV (post-electroporation) decreased 2-fold to 51% viability (**$p < 0.01$). These results validated that the electroporation processes may cause undesirable consequences, such as aggregation, resulting in high cytotoxicity. Therefore, it highlighted the need for investigating ***the aggregation effects post-electroporation*** as well as ***optimization of the electroporation processes*** to avoid any adverse effects on the cells, which are discussed below in two sub-sections.

3.5.1. Aggregation evaluation by spectroscopic assays and microscopy image analysis

To quantitatively determine the degree of aggregation post-electroporation, we used spectrometry and microscopy techniques. **Fig. S16A** shows the UV–Visible spectra of siRNA, EV, and various lipid-doped eEVs. In all cases, the samples were electroporated either with ("+siRNA") or without siRNA ("vesicle only"). The Opti-MEM and pre-electroporated eEVs conditions were measured as baselines and their spectra appear to overlap substantially. Because there was not a signature absorbance peak in the spectra (**Fig. S16A**), we used the maximum absorbance at 230 nm to quantify the aggregation as a turbidity measurement (Gregory (2009); Scherer et al., 2012), as shown in Fig. 5A. On the other hand, a few representative images for siRNA, EV w/o siRNA ("vesicle only"), and DOTAP-EV w/o siRNA ("vesicle only") are shown in **Fig. S16B** which were used for the microscopy image analysis. The results from both experiments showed the electroporation-induced aggregation occurred in not only membrane vesicles but also naked nucleic acids (siRNA). These finding were in line with previous observation from Stapulionis, R. J. B. (Stapulionis (1999)) and Kooijmans, S. A., *et al.* (Kooijmans et al., 2013). Notably, the quantitative results of turbidity (OD: 230 nm) (Fig. 5A) and semi-quantified image data (**Fig. S17**) showed a decrease of the tendency of aggregation when the electroporation is carried out in the presence of both siRNA and vesicles, compared to electroporating vesicles/siRNA alone. Moreover, the data suggest that in most cases, the degree of aggregate formation decreased for all lipid-doped eEVs, compared to native EVs post-electroporation. A larger library of lipids would need to be assessed in order to elucidate the entire parameters affecting the aggregation, however.

We also validated the aggregation of siRNA loaded EVs/eEVs, in terms of the turbidity (OD: 230 nm), number, and the size of aggregates. We found the results vary in a concentration-dependent manner for all EV/eEV formulations. Our data demonstrated the degree of aggregation (Fig. 5B, C, and D's y-axis are OD: 230 nm, aggregate concentration, and size, respectively) significantly increased 9- to 17-fold at the concentrations used for DLS and cell studies ($> 10^{10}$ particles/ml), in comparison to the sample concentration used for NTA measurement (10^{8} particles/ml). These findings point out the electroporation-caused aggregation may be far more significant than previously believed. Given that NTA is commonly used for particle analysis in the scientific community at a concentration of approximately hundred-fold lower than the dose applied for cell studies, the aggregation effects are likely underestimated. We provided evidence that strong aggregation of samples occurs after electroporation, which may result in far more severe impacts for *in vitro* and *in vivo* studies than NTA appears to be suggesting.

3.5.2. Optimization of the electroporation processes for efficient cargo loading and alleviation of the electroporation-caused aggregation and cytotoxicity

Because we have validated substantial aggregation of EV/eEV and siRNA was formed following electroporation, we endeavored to mitigate the toxicity by tuning the electroporation conditions. Several studies have reported a numbers of electroporation parameters could greatly influence the loading efficiency and aggregation results, such as applied voltage (Lamichhane et al., 2015; Stapulionis (1999)), pulse type (Lamichhane et al., 2015), pulse number (Lamichhane et al., 2015), and electroporation media (Hood et al., 2014; Kooijmans et al., 2013). Here, we focused our efforts on the parameter specific to the electroporation buffer.

We evaluated the aggregation effects of various electroporation media (Opti-MEM + EDTA, 50 mM trehalose, and hypotonic electroporation buffer) after electroporation. We demonstrated the aggregation can be remarkedly decreased by adding EDTA to electroporation buffer (Fig. 6A), as suggested in previous literature (Kooijmans et al., 2013; Stapulionis (1999)). However, unfortunately, the microscope

imaging results confirmed the submicron aggregates were not removed and yet still existed in substantial amounts by microscopy image analysis (**Fig. S18**). More strikingly, the effects of 50 mM trehalose on the aggregation level appeared to be different for different lipid-type eEVs. While the aggregation level of DPPC-EV, POPG-EV and native EV tended to decrease in 50 mM trehalose following electroporation, unexpectedly, the aggregation of DOTAP-EV and POPC-EV were likely to increase (Fig. 6A). These results are opposite to the hypothesis from Hood, J. L., et al. who reported that a 50 mM trehalose solution may minimize aggregate formation following electroporation (Hood et al., 2014), suggesting different concentration of trehalose solution may be needed for different lipid-doped eEV system to optimize the aggregation effects. Moreover, despite hypotonic electroporation buffers are being commonly used in several studies for electroporation, we demonstrated the aggregation of eEVs in hypotonic electroporation buffers following electroporation was at least 1.5-fold higher than the eEVs in Opti-MEM (Fig. 6A). This discrepancy of results compared to previous literature could be attributed to the differences of employed assays for aggregation evaluation. While most studies used NTA measurement as a mean to determine the size and numbers of aggregates, the sub-visible aggregates may be underestimated, as discussed in the previous section. Regarding metabolic activity of EV/eEV while varying the electroporation buffers (Fig. 6B), the 50 mM trehalose formulation was affiliated with the highest viability, except for POPG-EV (no statistical difference). In all cases, the formulations using Opti-MEM were significantly more toxic than the other buffers, which was 2-fold more toxic than using Opti-MEM + EDTA and 50 mM trehalose. Taken together, it is interesting to note that our results demonstrated the degree of aggregation of electroporated mixture may not be a direct linear relationship corresponding to cytotoxicity. Here, we also demonstrated the trend of cell viability with the variation of aggregation by combining the data from various media. **Fig. S19** highlighted the correlation of aggregation for eEV appeared to be biphasic in response to cell viability, while the most toxic regime showed in the range of 0.2 – 0.4 measured absorbance (OD: 230 nm). Importantly, it should be noted that elucidating whether aggregation and cytotoxicity are correlative, or causative would be challenging, as aggregation is a secondary variable dependent on other factors. In other words, we cannot hold all other variables constant while varying aggregation to assess its effects on cytotoxicity alone. It is important to note that the cytotoxicity profiles of eEVs on non-cancerous cells were also examined in this study. No toxicity was observed on healthy cells using the optimized electroporation buffer (**Fig. S20**). Given that the promise of electroporation continues to be hampered by a lack of appropriate and optimized conditions, we believe investigating these parameters could be helpful for future consideration of EV-based gene therapies and enhance the potential clinical translation of EVs.

3.6. Quantification of RNAi knockdown and eEV targetability

We opted to assess the siRNA silencing effects of EVs and eEVs electroporated in both Opti-MEM media with EDTA addition and 50 mM trehalose with the formulations which were affiliated with a cell viability greater than 80% (Fig. 6B). Fig. 7A qualitatively demonstrated the decrease in the total GFP expression in the cells. To quantify the GFP expression in cells, fluorescence intensity was monitored over time using a plate reader assay. Fig. 7B-D quantified the overall knockdown efficiency by analyzing the area under the curve for knockdown over time. Using 100 µl Opti-MEM, 10^{11} particles/ml, and 1 ng/µl siRNA in Opti-MEM, a 10 – 46% of knockdown efficiency was able to achieve by the eEV formulations, whereas the native EV-delivered siRNA failed to knockdown the GFP expression in an effective manner (**Fig. S21A**). An early and rapid decrease of knockdown efficiency was observed in native EV treated group at day 2, while the knockdown efficiency dropped after day 4 in eEVs. Overall, zwitterionic POPC-EV showed a highest knockdown with 41.1 ± 9.8% at 4 days post-transfection, which was comparable to commercial Lipofectamine RNAiMax of 43.3 ± 0.3% (**Fig. S21B and C**). A summary of the overall knockdown efficiency in Fig. 7B showed the knockdown efficiency of POPC-EV over time was statistically greater than the knockdown efficiency of EV (****$p < 0.0001$). Next, the experiments were repeated using anionic POPG-EV to deliver the siRNAs to the cells with different dosage. Despite only 21% of knockdown was achieved by POPG-EV with initial dosage, **Fig. S22A** showed that high dose of eEVs can more effectively down regulate the expression of GFP. A 2.4-fold of increase in inhibition of GFP expression was observed for 4-fold amount of dose of POPG-EV compared to initial dose. No statistical difference was observed between the area under curve of POPG-EV with the amounts of 4-fold dose and commercial Lipofectamine RNAiMax (Fig. 7C). The knockdown results among different lipid-doped eEVs implied the minimum effective dosage required varied with the properties of hybridized lipids. Further evaluation on the dosage effect would be worthwhile in future studies.

On the other hand, for the knockdown results of EVs and eEVs electroporated in 50 mM trehalose (**Fig. S22B**), the extent of knockdown of EV increased to 22–34% knockdown compared to the knockdown results (< 10%) electroporated in Opti-MEM. These results could potentially be attributed to the decrease of aggregation for EV in trehalose. However, like the aggregation data shown in Fig. 6E and F, the effects of the electroporation buffer on knockdown also differed between different lipid-doped eEVs. A significant increase of knockdown efficiency to 49.0% ± 7.3% was observed in the cells treated with cationic DOTAP-EV in 50 mM trehalose at 4 days post-transfection, while POPC-EV failed to reach 10% knockdown of the GFP expression (**Figure S22B**). The overall knockdown efficiency of eEVs in Trehalose (Fig. 7D) shows only the knockdown efficiency of DOTAP-EV over time was comparable to the knockdown efficiency of commercial Lipofectamine RNAiMax (no statistical difference) and greater than the knockdown efficiency of EV (*$p < 0.05$) in this case.

While discussing the functionality and efficacy of eEVs using different electroporated media, it should be noted that the findings of electroporation-induced aggregation pointed out a complication regarding the determination of knockdown efficiency; aggregated and precipitated particles may be uptake differently by the cells and may not be easily removed by washing. Therefore, it can be mistakenly considered as being transfected into the cells (Stapulionis (1999)). Further, to the extent of our knowledge, the scientific community has not conducted experiments to determine whether such aggregates inhibit or enhance the EV-mediated siRNA delivery into the cells (Kooijmans et al., 2013). Aggregation is known, however, in previous studies to cause enhanced uptake in at least certain cases (Cho et al., 2011). Interestingly, by assessing the knockdown effects of lipid-siRNA complexes, which were the same lipids we used in our studies for doping purposes, we found RNAi only occurred when lipids POPC, POPG and DPPC were fused into EV vesicle membrane. As shown in Fig. 7E, siRNA complexes with lipid POPC, POPG and DPPC was not able to down-regulate GFP expression. These results suggest the lipoplexes which may form would not have contributed to the knockdown observed for POPC, POPG, and DPPC lipid-doped eEVs.

To further investigate if lipid-doped eEVs can direct targeting to different cell lines, we quantified the cellular uptake of native EVs and eEVs in lung adenocarcinoma (A549) and lung normal fibroblast (CCL-210). Prior to the uptake studies, Deep Red membrane dye was used to stain the exosomal membrane of EVs/eEVs, followed by incubation with the cells. The confocal images of cellular uptake (Fig. 8A) revealed the internalization and localization of vesicles (red) in the cytoplasmic area. To further quantify the uptake efficiency between cell lines, flow cytometry assay was conducted and demonstrated in Fig. 8B. We observed significant differences in EV uptake between the two cell lines, with the most efficient cell line, lung adenocarcinoma (A549), demonstrating a 15.8-fold higher uptake amount compared to the normal lung fibroblast (CCL-210). Remarkably, A549 cells also showed an

increased propensity to take up eEVs that a 14.2-fold higher eEV uptake efficiency by A549 cells than that by CCL-210 cells was observed. Moreover, A549 cells exhibited a higher percentage of uptake population than CCL-210 cells. Approximately 84.2% of A549 cells were uptake with eEVs, whereas only 47.8% of CCL-210 cells were uptake with eEVs (Fig. 8C). Taken together, we observed a universal increase in uptake efficiency for the lung cancer cells versus normal lung fibroblast. These results supported the conclusion that the lipid-doped eEVs retained the targetability of EVs, despite the degree of selectivity on the cell lines could be declined by the decrease of EV portion in the engineered vesicle membrane. In this study, how precisely the engineered lipid-doped eEVs entered the cells and how knockdown is achieved are yet needed to be investigated. We opted to test the cellular internalization of eEVs using zwitterionic POPC-EV because of the high knockdown efficiency (Fig. 7B) and because little to no gene delivery effect was found from POPC lipid-siRNA complexes in our previous evaluation (Fig. 7E) that the cellular internalization would less likely be affected by any free lipid components. Nevertheless, more research should be done in near future in terms of the uptake mechanisms (*i.e.* clathrin- and caveolae-mediated endocytosis, macropinocytosis) to elucidate the critical factors determining EVs/eEVs uptake and targeting at molecular structure levels.

4. Conclusions

Despite there being increasingly more research advances in EV-mediated gene delivery, a key problem for EVs in clinical applications is the lack of methods for obtaining large-scale amounts of EV for practical use (Armstrong and Stevens, 2018). Although MSCs are commonly used for this reason, MSCs are not the most desirable cell types in all applications. In this study, we sought to: establish a simple synthetic lipid fusion technique which can be potentially applied to any lipid of interest; to quantify the level of native protein remaining; and to quantify the levels of gene knockdown, with acceptable levels of toxicity. We were successful in accomplishing these objectives using sonication and extrusion techniques to engineer EVs after isolation. We were able to achieve an 8-fold higher in the vesicle number over the common EV mass production method, while retaining 16 – 21% of native EV protein.

It is currently unknown what the balance is regarding how low the protein amount on the eEVs can be, while retaining targeting functionality. We currently have plans to investigate the sufficient levels of native protein remaining on eEVs to retain targeting functionality. Additionally, EVs derived from the cells may contain endogenous microRNA messages, which depends on the cell status and could be a concern of causing additional cell reactions. Therefore, to efficiently engineer EVs as a drug delivery platform by “voiding” the endogenous materials in the vesicles, while retaining the membrane structure and the capability of exogenous cargo loading, is our next step for EV-based drug delivery researches.

Furthermore, we found during our studies that electroporation causes an increase in the aggregation and toxicity but that such effects can be ameliorated to a degree by varying the electroporation media. We have evaluated the effects and the correlation of different electroporation buffer with aggregation. By optimizing the aggregation of eEVs, we have demonstrated the resulting lipid-doped eEVs are able to induce effective gene silencing as well as actively target to the cancer cells.

Other future studies will include the degree of lamellarity within our eEVs, as well as layer-by-layer applications which could potentially incorporate complexed or conjugated small molecules for anti-cancer applications. Additionally, the continued development of exogenous cargo loading methods, such as incorporating hydrophobic, cholesterol modified-siRNA (hsiRNA) (Haraszti et al., 2018a; O’Loughlin et al., 2017) into lipid-doped eEV system or using sonication method (Lamichhane et al., 2016), to maximize siRNA loading efficiency, in preparation for *in vivo* gene silencing effects for demonstrating clinical utility. Given that we have demonstrated the proof-of-principle, we will also be taking more of a high throughput approach in the future which could potentially be used to optimize targeting and gene delivery for any cell type of interest. To the extent of our knowledge, this is the first study investigating a variety of different lipids for EV fusion intended for mass production and knockdown of a gene of interest.

Declaration of Competing Interest

The authors declare that they have no known competing financial interests or personal relationships that could have appeared to influence the work reported in this paper.

Acknowledgements

We would like to acknowledge the Microscopy and Imaging center for supporting our TEM measurements and Texas A&M Institute of Genomic Medicine (TIGM) for supporting our electroporation experiments. This work was supported by the Taiwanese study abroad fellowship and by the department of Biomedical Engineering at Texas A&M University.

Appendix A. Supplementary material

Supplementary data to this article can be found online at https://doi.org/10.1016/j.ijpharm.2019.118802.

References

Alvarez-Erviti, L., Seow, Y., Yin, H., Betts, C., Lakhal, S., Wood, M.J., 2011. Delivery of siRNA to the mouse brain by systemic injection of targeted exosomes. Nat. Biotechnol. 29, 341–345.

Andaloussi, S.E., Lakhal, S., Mäger, I., Wood, M.J., 2013a. Exosomes for targeted siRNA delivery across biological barriers. Adv. Drug Deliv. Rev. 65, 391–397.

Andaloussi, S.E., Mäger, I., Breakefield, X.O., Wood, M.J., 2013b. Extracellular vesicles: biology and emerging therapeutic opportunities. Nat. Rev. Drug Discovery 12, 347–357.

Antimisiaris, S., Mourtas, S., Papadia, K., 2017. Targeted si-RNA with liposomes and exosomes (extracellular vesicles): how to unlock the potential. Int. J. Pharmac. 525, 293–312.

Armstrong, J.P., Holme, M.N., Stevens, M.M., 2017. Re-Engineering extracellular vesicles as smart nanoscale therapeutics. ACS Nano 11, 69–83.

Armstrong, James P.K., Stevens, Molly M., 2018. Strategic design of extracellular vesicle drug delivery systems. Adv. Drug Deliv. Rev. 130, 12–16. https://doi.org/10.1016/j.addr.2018.06.017.

Bishop, C.J., Tzeng, S.Y., Green, J.J., 2015. Degradable polymer-coated gold nanoparticles for co-delivery of DNA and siRNA. Acta Biomater. 11, 393–403.

Charoenphol, Phapanin, Oswalt, Katie, Bishop, Corey J., 2018. Therapeutics incorporating blood constituents. Acta Biomater. 73, 64–80. https://doi.org/10.1016/j.actbio.2018.03.046.

Cho, E.C., Zhang, Q., Xia, Y., 2011. The effect of sedimentation and diffusion on cellular uptake of gold nanoparticles. Nature Nanotechnol. 6, 385.

Christianson, H.C., Svensson, K.J., van Kuppevelt, T.H., Li, J.-P., Belting, M., 2013. Cancer cell exosomes depend on cell-surface heparan sulfate proteoglycans for their internalization and functional activity. Proc. Natl. Acad. Sci. 110 (43), 17380–17385. https://doi.org/10.1073/pnas.1304266110.

Conlan RS, Pisano S, Oliveira MI, Ferrari M, Pinto IM. 2017. Exosomes as reconfigurable therapeutic systems. 23, 636-650.

El-Andaloussi, S., Lee, Y., Lakhal-Littleton, S., Li, J., Seow, Y., Gardiner, C., Alvarez-Erviti, L., Sargent, I.L., Wood, M.J., 2012a. Exosome-mediated delivery of siRNA in vitro and in vivo. Nat. Protoc. 7, 2112.

El-Andaloussi S, Lee Y, Lakhal-Littleton S, Li J, Seow Y, Gardiner C, Alvarez-Erviti L, Sargent IL, Wood MJ., 2012b. Exosome-mediated delivery of siRNA in vitro and in vivo. 7, 2112.

Fuhrmann, G., Chandrawati, R., Parmar, P.A., Keane, T.J., Maynard, S.A., Bertazzo, S., Stevens, M.M.J.A.M., 2018. Engineering extracellular vesicles with the tools of enzyme prodrug. Therapy. 30, 1706616.

Gilligan, K.E., Dwyer, R.M., 2017. Engineering exosomes for cancer therapy. Int. J. Mol. Sci. 18, 1122.

Golzio M, Mora MP, Raynaud C, Delteil C, Teissié J, Rols MP. 1998. Control by osmotic pressure of voltage-induced permeabilization and gene transfer in mammalian cells. 74, 3015-3022.

Greening, D.W., Xu, R., Ji, H., Tauro, B.J., Simpson, R.J., 2015. A protocol for exosome isolation and characterization: evaluation of ultracentrifugation, density-gradient separation, and immunoaffinity capture methods. Proteomic Profiling. Springer

179–209.
Gregory, J.J.A.i.c., science, i., 2009. Monitoring particle aggregation processes. 147, 109-123.
Haraszti, R.A., Miller, R., Didiot, M.-C., Biscans, A., Alterman, J.F., Hassler, M.R., Roux, L., Echeverria, D., Sapp, E., DiFiglia, M., 2018a. Optimized cholesterol-siRNA chemistry improves productive loading onto extracellular vesicles. Mol. Ther. 26, 1973–1982.
Haraszti, R.A., Miller, R., Stoppato, M., Sere, Y.Y., Coles, A., Didiot, M.-C., Wollacott, R., Sapp, E., Dubuke, M.L., Li, X.J.M.T., 2018b. Exosomes Produced from 3D Cultures of MSCs by Tangential Flow Filtration Show Higher Yield and. Improved Activity.
Harding CV, Heuser JE, Stahl PD. 2013. Exosomes: looking back three decades and into the future. 200, 367-371.
Hood, J.L., Scott, M.J., Wickline, S.A., 2014. Maximizing exosome colloidal stability following electroporation. Anal. Biochem. 448, 41–49.
Jamaluddin MP, Krishman LK. 1987. A spectrophotometric method for following initial rate kinetics of blood platelet aggregation. 14, 191-200.
Jang, S.C., Kim, O.Y., Yoon, C.M., Choi, D.-S., Roh, T.-Y., Park, J., Nilsson, J., Lötvall, J., Kim, Y.-K., Gho, Y.S., 2013. Bioinspired exosome-mimetic nanovesicles for targeted delivery of chemotherapeutics to malignant tumors. ACS Nano 7, 7698–7710.
Jiang, X.-C., Gao, J.-Q., 2017. Exosomes as novel bio-carriers for gene and drug delivery. Int. J. Pharm. 521, 167–175.
Jiang XC, Gao JQ. 2017b. Exosomes as novel bio-carriers for gene and drug delivery. 521, 167-175.
Jin H, Bae Y, Kim M, Kwon SJ, Jeon H, Choi S, Kim S, Yang Y, Oh W, Chang J. 2013. Comparative analysis of human mesenchymal stem cells from bone marrow, adipose tissue, and umbilical cord blood as sources of cell therapy. 14, 17986-18001.
Kamerkar, S., LeBleu, V.S., Sugimoto, H., Yang, S., Ruivo, C.F., Melo, S.A., Lee, J.J., Kalluri, R.J.N., 2017. Exosomes facilitate therapeutic targeting of oncogenic KRAS in pancreatic cancer. 546, 498.
Kanada M, Bachmann MH, Hardy JW, Frimannson DO, Bronsart L, Wang A, Sylvester MD, Schmidt TL, Kaspar RL, Butte MJ, Matin AC. 2015. Differential fates of biomolecules delivered to target cells via extracellular vesicles. 201418401.
Kim, Y.-D., Park, T.-E., Singh, B., Maharjan, S., Choi, Y.-J., Choung, P.-H., Arote, R.B., Cho, C.-S., 2015. Nanoparticle-mediated delivery of siRNA for effective lung cancer therapy. Nanomedicine 10, 1165–1188.
Kooijmans, S.A., Stremersch, S., Braeckmans, K., de Smedt, S.C., Hendrix, A., Wood, M.J., Schiffelers, R.M., Raemdonck, K., Vader, P., 2013. Electroporation-induced siRNA precipitation obscures the efficiency of siRNA loading into extracellular vesicles. J. Control. Release 172, 229–238.
Lamichhane, T.N., Jeyaram, A., Patel, D.B., Parajuli, B., Livingston, N.K., Arumugasaamy, N., Schardt, J.S., Jay, S.M., 2016. Oncogene knockdown via active loading of small RNAs into extracellular vesicles by sonication. Cell. Mol. Bioeng. 9, 315–324.
Lamichhane, T.N., Raiker, R.S., Jay, S.M., 2015. Exogenous DNA loading into extracellular vesicles via electroporation is size-dependent and enables limited gene delivery. Mol. Pharm. 12, 3650–3657.
Lee, S.J., Kim, M.J., Kwon, I.C., Roberts, T.M., 2016. Delivery strategies and potential targets for siRNA in major cancer types. Adv. Drug Deliv. Rev. 104, 2–15.
Löf, L., Ebai, T., Dubois, L., Wik, L., Ronquist, K.G., Nolander, O., Lundin, E., Söderberg, O., Landegren, U., Kamali-Moghaddam, M., 2016. Detecting individual extracellular vesicles using a multicolor in situ proximity ligation assay with flow cytometric readout. Scientific reports 6, 34358.
Lu M, Zhao X, Xing H, Xun Z, Zhu S, Lang L, Yang T, Cai C, Wang D, Ding P. 2018. Comparison of exosome-mimicking liposomes with conventional liposomes for intracellular delivery of siRNA. 550, 100-113.
Luan, X., Sansanaphongpricha, K., Myers, I., Chen, H., Yuan, H., Sun, D., 2017. Engineering exosomes as refined biological nanoplatforms for drug delivery. Acta Pharmacol. Sin. 38, 754.
Lv, H., Zhang, S., Wang, B., Cui, S., Yan, J., 2006. Toxicity of cationic lipids and cationic polymers in gene delivery. J. Control. Release 114, 100–109.
Maas, S.L., Breakefield, X.O., Weaver, A.M., 2017. Extracellular vesicles: unique intercellular delivery vehicles. Trends Cell Biol. 27, 172–188.
Maheshwari, R., Tekade, M., Gondaliya, P., Kalia, K., D'Emanuele, A., Tekade, R.K., 2017. Recent advances in exosome-based nanovehicles as RNA interference therapeutic carriers. Nanomedicine 12, 2653–2675.
Marimpietri, D., Petretto, A., Raffaghello, L., Pezzolo, A., Gagliani, C., Tacchetti, C., Mauri, P., Melioli, G., Pistoia, V., 2013. Proteome profiling of neuroblastoma-derived exosomes reveal the expression of proteins potentially involved in tumor progression. PLoS ONE 8, e75054.
Mitchell, J.P., Court, J., Mason, M.D., Tabi, Z., Clayton, A., 2008. Increased exosome production from tumour cell cultures using the Integra CELLine Culture System. J. Immunol. Methods 335, 98–105.
Navakanitworakul, R., Hung, W.-T., Gunewardena, S., Davis, J.S., Chotigeat, W., Christenson, L.K., 2016. Characterization and small RNA content of extracellular vesicles in follicular fluid of developing bovine antral follicles. Sci. Rep. 6, 25486.
O'Loughlin, A.J., Mäger, I., de Jong, O.G., Varela, M.A., Schiffelers, R.M., El Andaloussi, S., Wood, M.J., Vader, P., 2017. Functional delivery of lipid-conjugated siRNA by extracellular vesicles. Mol. Ther. 25, 1580–1587.
Ohno, S.-I., Drummen, G.P., Kuroda, M., 2016. Focus on extracellular vesicles: development of extracellular vesicle-based therapeutic systems. Int. J. Mol. Sci. 17, 172.
Osteikoetxea, X., Balogh, A., Szabó-Taylor, K., Németh, A., Szabó, T.G., Pálóczi, K., Sódar, B., Kittel, Á., György, B., Pállinger, É., 2015. Improved characterization of EV preparations based on protein to lipid ratio and lipid properties. PLoS ONE 10, e0121184.
Pi F, Binzel DW, Lee TJ, Li Z, Sun M, Rychahou P, Li H, Haque F, Wang S, Croce CM, Guo B. 2018. Nanoparticle orientation to control RNA loading and ligand display on extracellular vesicles for cancer regression. 13, 82.
Piffoux, M., Silva, A.K., Wilhelm, C., Gazeau, F., Tareste, D.J.A.n., 2018. Modification of Extracellular Vesicles by Fusion with Liposomes for the Design of Personalized Biogenic Drug Delivery Systems. 12, 6830-6842.
Properzi, F., Logozzi, M., Fais, S., 2013. Exosomes: the future of biomarkers in medicine. Biomarkers Med. 7, 769–778.
Rana, S., Yue, S., Stadel, D., Zöller, M., 2012. Toward tailored exosomes: the exosomal tetraspanin web contributes to target cell selection. Int. J. Biochem. Cell Biol. 44, 1574–1584.
Ren, J., He, W., Zheng, L., Duan, H., 2016. From structures to functions: insights into exosomes as promising drug delivery vehicles. Biomater. Sci. 4, 910–921.
Ruigrok, M., Frijlink, H., Hinrichs, W., 2016. Pulmonary administration of small interfering RNA: The route to go? J. Control. Release 235, 14–23.
Sato, Y.T., Umezaki, K., Sawada, S., Mukai, S.-A., Sasaki, Y., Harada, N., Shiku, H., Akiyoshi, K., 2016. Engineering hybrid exosomes by membrane fusion with liposomes. Sci. Rep. 6, 21933.
Scherer, T.M., Leung, S., Owyang, L., Shire, S.J.J.T.A.j., 2012. Issues and challenges of subvisible and submicron particulate analysis in protein solutions. 14, 236-243.
Srivastava, A., Babu, A., Filant, J., Moxley, K.M., Ruskin, R., Dhanasekaran, D., Sood, A.K., McMeekin, S., Ramesh, R., 2016. Exploitation of exosomes as nanocarriers for gene-, chemo-, and immune-therapy of cancer. J. Biomed. Nanotechnol. 12, 1159–1173.
Stapulionis, R.J.B., bioenergetics, 1999. Electric pulse-induced precipitation of biological macromolecules in electroporation. 48, 249-254.
Sun, D., Zhuang, X., Zhang, S., Deng, Z.-B., Grizzle, W., Miller, D., Zhang, H.-G., 2013. Exosomes are endogenous nanoparticles that can deliver biological information between cells. Adv. Drug Deliv. Rev. 65, 342–347.
Szatanek, R., Baran, J., Siedlar, M., Baj-Krzyworzeka, M., 2015. Isolation of extracellular vesicles: determining the correct approach. Int. J. Mol. Med. 36, 11–17.
Takov, K., Yellon, D.M., Davidson, S.M., 2017. Confounding factors in vesicle uptake studies using fluorescent lipophilic membrane dyes. J. Extracellular Vesicles 6, 1388731.
Théry, C., Amigorena, S., Raposo, G., Clayton, A., 2006. Isolation and characterization of exosomes from cell culture supernatants and biological fluids. Current protocols in cell biology, 3.22. 21-23.22. 29.
Tran, T.-H., Mattheolabakis, G., Aldawsari, H., Amiji, M., 2015. Exosomes as nanocarriers for immunotherapy of cancer and inflammatory diseases. Clinical Immunol. 160, 46–58.
Turinetto V, Vitale E, Giachino C. 2016. Senescence in human mesenchymal stem cells: functional changes and implications in stem cell-based therapy. 17, 1164.
Usaj M, Kanduser M. 2012. The systematic study of the electroporation and electrofusion of B16-F1 and CHO cells in isotonic and hypotonic buffer. 245, 583-590.
Ušaj, M., Trontelj, K., Hudej, R., Kandušer, M., Miklavčič, D.J.R., Oncology, 2009. Cell size dynamics and viability of cells exposed to hypotonic treatment and electroporation for electrofusion optimization. 43, 108-119.
Vader, P., Mol, E.A., Pasterkamp, G., Schiffelers, R.M., 2016. Extracellular vesicles for drug delivery. Adv. Drug Deliv. Rev.
Watson, D.C., Bayik, D., Srivatsan, A., Bergamaschi, C., Valentin, A., Niu, G., Bear, J., Monninger, M., Sun, M., Morales-Kastresana, A.J.B., 2016. Efficient production and enhanced tumor delivery of engineered extracellular vesicles. 105, 195–205.
Xu, R., Greening, D.W., Zhu, H.-J., Takahashi, N., Simpson, R.J., 2016. Extracellular vesicle isolation and characterization: toward clinical application. Journal of Clinical Investigation 126, 1152.
Yeo RW, Lai RC, Zhang B, Tan SS, Yin Y, Teh BJ, Lim SK., 2013. Mesenchymal stem cell: an efficient mass producer of exosomes for drug delivery. 65, 336-341.
Zhang Q, Ran R, Zhang L, Liu Y, Mei L, Zhang Z, Gao H, He Q. 2015. Simultaneous delivery of therapeutic antagomirs with paclitaxel for the management of metastatic tumors by a pH-responsive anti-microbial peptide-mediated liposomal delivery system. 197, 208-218.